$Ti_3C_2T_x$ MXene core-shell spheres for ultrahigh removal of mercuric ions

Asif Shahzad[1], Mohsin Nawaz[1], Mokrema Moztahida[1], Jiseon Jang[2], Khurram Tahir[1], Jiho Kim[1], Youngsu Lim[1], Vassilios S. Vassiliadis[3], Seung Han Woo[4,*] and Dae Sung Lee[1,*]

[1]*Department of Environmental Engineering, Kyungpook National University, 80 Daehak-ro, Buk-gu, Daegu 41566, Republic of Korea*

[2]*R&D Institute of Radioactive Wastes, Korea Radioactive Waste Agency, 174 Gajeong-ro, Yuseong-gu, Daejeon 34129, Republic of Korea*

[3]*Department of Chemical Engineering and Biotechnology, University of Cambridge, West Cambridge Site, Philippa Fawcett Drive, Cambridge CB3 0AS, UK*

[4]*Department of Chemical Engineering, Hanbat National University, 125 Dongseodae-ro, Yuseong-gu, Daejeon 34158, Republic of Korea*

*To whom all correspondence should be addressed.

Tel.: +82-53-953-7286; Fax: +82-53-950-6579

E-mail: daesung@knu.ac.kr & shwoo@hanbat.ac.kr

Abstract

Two-dimensional (2-D) titanium carbide MXene core ($Ti_3C_2T_x$) shell aerogel spheres (MX-SA) for mercuric ion removal were designed and fabricated with varying concentrations of $Ti_3C_2T_x$ MXene and sodium alginate (SA) using a facile method. Owing to their unique inside structures, high porosities, large specific surface areas, oxygenated functional groups of MXene nanosheets, and available active binding sites, the synthesized microspheres constitute a unique adsorbent for heavy metals removal in water. The MX-$SA_{4:20}$ spheres exhibit an exceptional adsorption capacity of 932.84 mg/g for Hg^{2+}, which is among the highest value reported for adsorbents. The adsorbent exhibits high single- and multi-component removal efficiencies, with 100% efficiency for Hg^{2+} and > 90% efficiency for five heavy metal ions. The synthesized materials are highly efficient for Hg^{2+} removal under extreme pH conditions (0.5–1.0 M HNO_3) and have additional excellent reproducible properties. The micro-size and spherical shape of MX-$SA_{4:20}$ also allow it to be used in column-packed devices.

Keywords: Titanium carbide; Microspheres; Adsorption; Heavy metal

1. Introduction

With water scarcity and pollution representing global concerns in the twenty-first century [1–3], the presence of heavy metals in water constitutes a serious risk to humans and other life forms on Earth [4,5]. Mercury (Hg) is known to be one of the most poisonous heavy metals both in water and air environments [6–8], as a result of its persistence, bioaccumulation, and volatile nature, poses a large potential health threat to living organisms [9,10]. It is therefore of cardinal importance to address the issue of Hg contamination in waste and drinking water [11,12]. Among the technologies currently being used for heavy metal ion treatment, adsorption is considered to be the most useful and practical owing to its simplicity and effectiveness [13–16]. A large and diverse (in terms of sorption activities toward mercuric ions) set of adsorbents has been synthesized and assessed to date. Ion exchange resins [17], activated carbon [18], metal organic frameworks (MOFs) [19,20], and thiol-functionalized materials such as functionalized clay [21–23], have all shown exceptionally high adsorption capacities. However, such materials suffer from low functional densities, improper distributions of functional groups on their sorbents, stability issues, low surface areas, and/or small pore sizes [24], These undesirable characteristics are compounded by the need for multiple-step, complex synthesis procedures and costly feedstock chemicals such as organic ligands for COFs synthesis [19,25]. Engineered nanomaterials, particularly two-dimensional (2-D) nanomaterials, with unique physical and chemical properties such as unsaturated surface atoms and greater surface energy fractions, offer an alternative for effectively adsorbing heavy metals such as Hg(II) [26]. One example of these substances is the recently invented 2-D MXenes ($M_{n+1}X_nT_x$) [27]. 2-D Titanium carbide ($Ti_3C_2T_x$), a member of the MXene family, has shown promise for use in antibacterial activates [28], fouling-resistant membranes [29], and heavy metal decontamination [30,31]. $Ti_3C_2T_x$ MXene nanosheets are an expanding class of 2-D nanomaterials that offer post-synthesis surface engineering capability, tunable chemistry, hydrophilic surfaces, and high surface areas [32,33]. Previously, the authors reported on the extraordinarily high affinity of $Ti_3C_2T_x$-based nanocomposite (*MGMX*) for Hg^{2+} adsorption [31]. However, long-term stability issues, low

porosity, and proneness to oxidation mean that it is impractical to continuously use $Ti_3C_2T_x$ in large-scale applications. Increasing the industrial-scale applicability of $Ti_3C_2T_x$ nanosheets will require the development of more stable and highly porous $Ti_3C_2T_x$-based materials for use in large-scale applications involving continuous operation, i.e., fixed-bed columns.

Hydrofluoric acid (HF) has been used extensively to exfoliate MAX phases but HF is an extremely hazardous material that causes serious environmental pollution and very harmful to health [27]. LiF with HCl has been proven as a relatively less toxic and mild etching agent for MAX phase exfoliations than HF, but long time reaction, multi-step synthesis process, and high operating temperature could limited its application to some extent [34]. Ammonium fluoride (NH_4F), on the other hand, is a less toxic and safe etching agent and has been also used to produce larger interplaner spacing $Ti_3C_2T_x$ MXene nanosheets [35,36]. One potential enhancement is sodium alginate (SA), a naturally occurring biopolymer possessing the characteristics of hydrogels with multivalent cations, that has been used widely in the entrapment of adsorbents in environmental applications [37]. SA is biocompatible, biodegradable, non-toxic, and available on a large scale; these are key features for its successful use in wastewater remediation applications [37]. Especially, carboxylate functional groups of the alginate polymer can form biodegradable gels in the presence of polyvalent cations, which make SA unique over other existing biopolymers such as cellulose and its derivatives [38].

In this study, $Ti_3C_2T_x$-filled spheres containing sodium alginate (MX-SA) were prepared at different weight ratios (% w/w) by deposition into calcium chloride aqueous solutions (with the divalent Ca^{2+} cation serving as a crosslinking agent). The spheres were shown to contain unique internal structures and exhibited an exceptional saturation Hg^{2+} uptake capacity of 932.84 mg/g. Although a mild, reduced-toxicity etching agent (NH_4F) was used in the $Ti_3C_2T_x$ nanosheets synthesis process, the result was a high quality product. The accessibility of Hg^{2+} ions to adsorbent binding sites was also assessed in terms of kinetics, adsorption capacity, pH involvement, and mass

transportation rates in the porous structure of adsorbent. Finally, the physical and chemical properties of the new adsorbent were analyzed.

2. Materials and Methods

2.1. Material

Titanium (-325 mesh, 99.0%), graphite powder (-325 mesh, 99.0%, Alfa Aeser), ammonium fluoride (NH_4F), arsenic oxide (AsO_3), chromium chloride ($CrCl_3$), and mercury chloride ($HgCl_2$) were purchased from Alfa Aeser, South Korea. Aluminum (-325 mesh, 99.7) was purchased from STEM Chemical INC. USA). Calcium chloride ($CaCl_2$), copper chloride ($CuCl_2$), lead chloride ($PbCl_2$), zinc nitrate ($Zn(NO_3)_2.6H_2O$), nickle nitrate ($Ni(NO_3)_2.6H_2O$), and cobalt nitrate ($Co(NO_3)_2.6H_2O$) was purchased from Daejung Chemicals, South Korea. $CdCl_2$ was acquired from Honeywell, South Korea.

2.2. 2-D $Ti_3C_2T_x$ (MXene) formation

Following the Ti_3AlC_2 MAX phase synthesis procedure explained in our previous work [32], $Ti_3C_2T_x$ MXene was synthesized using ammonium fluoride (NH_4F) as an etching agent. About 0.5 g of Ti_3AlC_2 powder (sieved with 200-mesh) was immersed slowly into 100 mL of 1-M NH_4F solution at room temperature (333 K) for 24 h. Following this, the mixture was washed with deionized water using vacuum filtration until a pH value of 6–7 was achieved. The filtrate was then dried in vacuum at 298 K to produce the synthesized $Ti_3C_2T_x$ MXene, which was stored for further use.

2.3. MX-SA sphere formation

MX-SA spheres were synthesized with different $Ti_3C_2T_x$ MXene and SA powder compositions. $Ti_3C_2T_x$ MXene powder was placed in pre-degassed deionized (DI) water and then ultrasonicated for 10 min under Ar gas to attain a homogenous dispersion of $Ti_3C_2T_x$ MXene multilayers. In

general, this process involved mixing 2.0 mg/mL $Ti_3C_2T_x$ MXene solution (50 mL) into 20 mg/mL SA (50 mL) solution followed by thorough dispersion under magnetic stirring. The aqueous MXene-alginate mixture was then injected as small droplets through a syringe needle (17 gauge) into a $CaCl_2$ (1.0 M, 200 mL) solution. A peristaltic pump connected to the tube controlled the flow rate of the solution (25 mL/min). The synthesized MX-$SA_{2:20}$ spheres were then stirred magnetically for 1 h, rinsed with DI water several times until a pH of 6.5–7 was attained, and then dried in a freeze dryer. Spheres with varying initial $Ti_3C_2T_x$ MXene concentrations (MX-$SA_{1:20}$, MX-$SA_{2:20}$, MX-$SA_{3:20}$, MX-$SA_{6:20}$, and GO-$SA_{4:20}$, where the subscripts denote the concentration of $Ti_3C_2T_x$ and SA in the mixed solution, respectively) were synthesized using the same protocol.

2.4. Sample Characterization

The samples were characterized via scanning electron spectroscopy (SEM) using a field emission scanning electron microscope (S-4800, HITACHI, Japan). The X-ray powder diffraction (XRD) spectra of the MX-$SA_{4:20}$ spheres were recorded using an XRD instrument (Rigaku D/MAX 2500PC powder XRD, 0.15418 nm Cu Kα radiation operating at 40 kV and 200 mA over a scanning range of 2–80°). Fourier-transform infrared spectroscopy (FTIR) spectra of the MX-$SA_{4:20}$ spheres were recorded in the 4,000–400 cm^{-1} spectral range using a spectrometer (Perkin–Elmer, USA). A scanning X-ray micrograph (SXM: ULVAC-PHI II, Quantera, Japan) was used to conduct X-ray photoelectron spectroscopy (XPS) to characterize the MX-$SA_{4:20}$ spheres. A Brunauer–Emmett–Teller (BET) analyzer was used to determine the surface area of the MX-$SA_{4:20}$ spheres while the Barrett−Joyner−Halen (BJH) method was applied using a Micromeritics ASAP-2020 analyzer with a nitrogen gas adsorption-desorption isotherm at 77 K to determine the pore size distribution. Thermo gravimetric analysis (TGA) under nitrogen gas was performed using a thermal analyzer system (TGA-DS, Q600 TA Instrument) at 23−1,000 °C with a heating flow rate of 10 °C min^{-1}.

2.5. Hg^{2+} Adsorption measurements

$HgCl_2$ salt was used to prepare a stock solution of 1000 mg/L mercuric ions (Hg^{2+}) in 3% HNO_3, which was then pH-adjusted using 0.1M/0.5M HNO_3 or NaOH. In a typical batch adsorption process, adsorbent was added into 30 mL of the Hg^{2+} solution at a concentration of 25 ppm (pH ~6.0) and agitated using a 180 rpm shaking incubator at 298 K for 24 h. Upon completion of the reaction, the remaining Hg^{2+} concentration was measured via inductively coupled plasma-optical emission spectrometry (ICP-OES) (ThermoFisher Scientific, Germany). The adsorbents' removal capacities for Hg^{2+} ion removal were quantified using equations given in Supplementary Information.

2.5.1. Kinetics measurements

Amount of 0.050 g/L MX-$SA_{4:20}$ sphere samples was added to a 25 ppm concentrated Hg^{2+} solution (pH 5.5), and agitated for several hours, with the samples filtered using a membrane filter at specific intervals. The filtrates were subjected to ICP-OES analysis to obtain the remaining concentration measurements.

2.5.2. Isotherm measurements

The ability of the MX-$SA_{4:20}$ samples to adsorb Hg^{2+} from water were determined using a batch adsorption system. 50 mg each of MX-$SA_{2:20}$ and MX-$SA_{4:20}$ spheres were added to 30 mL of various Hg^{2+} solutions (993.8, 695.66, 538, 405.6, 281.28, 198.12, 129.8, 64.61, and 31 ppm, respectively) under constant shaking at room temperature for 24 h. The initial and residual Hg^{2+} concentrations were determined using ICP-OES.

2.5.3. Multi-element system measurements

A 30 mL solution containing nine different metal ions (Hg^{2+}, Cd^{2+}, Cu^{2+}, Pb^{2+}, Zn^{2+}, Ni^{2+}, Co^{2+}, Cr^{3+}, and As^{3+}), each at a concentration of 3 ppm, was prepared and then 50 mg of MX-$SA_{4:20}$ was

introduced into the reaction bottle containing the metal ion solution. The reaction was allowed to proceed for 24 h under continuous agitation and the resulting solution was analyzed using ICP-OES. As a breakthrough experiment, 3.1 g of MX-$SA_{4:20}$ aerogel spheres were loaded into a column with a maximum bed height of 20 cm and a 1.5 cm inner dimeter to produce a dried adsorbent bed with a height of 12.5 cm that was then covered by glass wool. A multi-ion solution containing the nine elements listed above at 3 ppm concentrations and 4.67 ± 0.05 pH was then run through the column at room temperature at a flow rate of 0.3 mL/min using a Masterflex L/S digital pump. The samples were collected at different time intervals and subjected to ICP-OES analysis.

2.5.4. pH measurements

Typical batch adsorption experiments were carried out to investigate the effect of pH on the adsorption system. Several mixtures of 0.05 mg of MX-$SA_{4:20}$ spheres in Hg^{2+} (25 mg/L) solutions in 60 mL polypropylene tubes were prepared at initial pH ranges varying from 2–11. To further assess the Hg^{2+} adsorption in extreme pH conditions, mixing was also conducted in 0.5 and 1.0 molar HNO_3 solutions. After shaking the mixtures for 24 h, the Hg^{2+}-laden (Hg^{2+}@MX-$SA_{4:20}$) samples were analyzed using ICP-OES to measure the residual concentrations of Hg^{2+}.

2.5.5. Adsorbent comparison measurements

Typical batch adsorption experiments were performed to examine the Hg^{2+} adsorption effectiveness of different adsorbents. Fixed amounts of three adsorbents GO-$AS_{4:20}$, SA_{20}, and MX-$SA_{4:20}$ spheres, respectively, were added to 25 ppm 30 mL Hg^{2+} solutions and the reactions were allowed to proceed for 24 h, after which the residual metal ion concentrations were measured using ICP-OES.

3. Results and discussion

3.1. Preparation of $Ti_3C_2T_x$ spheres and morphology

2-D $Ti_3C_2T_x$ MXene-based spheres (MX-SA) were formed by dropping homogenous mixtures of $Ti_3C_2T_x$ and sodium alginate into a 1.0 M $CaCl_2$ solution, resulted in black-colored regular spheres. The structural morphology of synthesis sphere was studied by optical microscopy and scanning electron microscopy (SEM) techniques. The average diameter of spheres was 3.0 ± 0.2 mm and 2.1± 0.1 mm in wet and dry form, respectively (Fig. 1A and 1F). Examination of the morphologies and internal structures of the MX-$SA_{4:20}$ spheres (Fig. 1) via optimal microscopy revealed that the wet hydrogel spheres exhibited deceptively amorphous-like behavior, with internal structures not emerging until the spheres were dried (Fig. 1A and 1B).

Upon carving the spheres with a razor blade, revealed cross-sections with unambiguous core/shell structures observed by SEM images. The quite dense internal cores exhibited MXene-alginate amalgamation (Fig. 1D), while there were vacant spaces between the shell walls and inner cores (Fig. 1C, and 1G) that could only have been produced by a vacuum-freeze drying process, as processes such as air-drying in a high temperature oven under vacuum conditions cannot produce such unique structures. The average thicknesses of the inner cores and outer shell walls of the MX-$SA_{4:20}$ spheres were ~1.5 mm and ~20 µm, respectively (Fig. S1). Optical (Fig. 1C) and SEM (Fig. 1G) cross-sectional images of a vacuumed-freeze dried MX-$SA_{4:20}$ sample clearly revealed a self-structured core. Especially, $Ti_3C_2T_x$ MXene displayed a 2D nano-layered structure (Fig. 1E). Furthermore, SEM-energy dispersive spectroscopy measurements found increases in the C and O content relative to $Ti_3C_2T_x$ (from 11.31 and 13.47 wt% to 34.60 and 40.30 wt%, respectively) in the MX-$SA_{4:20}$ sample (Fig. S2). By contrast, very little Ti was found in the MX-$SA_{4:20}$ (3.32 wt%), although Cl and Ca were found to be present as a result of the complexation of alginate with calcium.

The XRD patterns (Fig. 2A) confirmed the successful production of 2-D $Ti_3C_2T_x$ MXene from the parent Ti_3AlC_2 MAX phase following extraction of the weakly bonded Al layers [39]. Treatment in a 1-M bifluoride (NH_4F) solution at 60 ^oC was sufficient to eliminate the entire Al from the MAX phase. A shift in a representative peak (002) from 9.5^o to a lower angle (7.16^o)

parallel to the *c* lattice parameter suggested the synthesis of larger interplaner spacing $Ti_3C_2T_x$ MXene [34,40]. Furthermore, the pristine alginate spheres demonstrated peak vibrations at 2θ values of $\sim 20^o$ [41]. In MX-$SA_{4:20}$, the appearance of the $Ti_3C_2T_x$ representative peak (002) at 6.98^o confirmed the synthesis of 3-D MXene-alginate network in the spheres, with the (002) peak shifting from 7.16 to 6.98^o suggesting an increase in interlayer spacing between the $Ti_3C_2T_x$ nanosheets, which was potentially attributable to the pristine MXene ultrasonication process during sphere synthesis [28]. Moreover, the intensity of the representative (002) peak increased with the $Ti_3C_2T_x$ MXene content in the MX-SA spheres in the order MX-$SA_{1:20}$ > MX-$SA_{1:20}$ > MX-$SA_{4:20}$ (Fig. S3). Further XPS analyses were conducted to confirm the successful synthesis and adsorption of Hg^{2+} onto the MX-$SA_{4:20}$ (Fig. 2B). The MX-$SA_{4:20}$ component spectra included typical $Ti_3C_2T_x$ MXene spectra for Ti_{2p}, C_{1s}, F_{1s}, and O_{1s} (Fig. S4 and S5). The emergence of F_{1s}, and O_{1s} and elimination of Al in the XPS scans confirmed the exfoliation of the MAX phase into the MXene [42]. In the MX-$SA_{4:20}$ XPS scans there was an addition of Cl_{1s} and Ca_{1s} component peaks as well as enhancements of C_{1s}, and O_{1s} components with respect to virgin MXene, which could be attributed to the addition of alginate into the heterostructural material. The component spectra could be decomposed into various peaks, namely, Ti_{2p} (5 peaks), C_{1s} (3 peaks), F_{1s} (2 peaks), O_{1s} (5 peaks), and Cl_{1s} (3 peaks). The binding energies of the respective peak fittings are shown in Table S1.

FTIR spectroscopy was used to determine the infrared absorption spectra of $Ti_3C_2T_x$, SA_{20}, MX-$SA_{4:20}$, and Hg^{2+}@MX-$SA_{4:20}$. These are shown in Fig. S6, from which it is seen that the composite spectra all have multiple major peaks in 4,000-400 cm^{-1} wavelength range. Note also that the IR spectra of MX-$SA_{4:20}$ are dissimilar to those of $Ti_3C_2T_x$, which has an enhanced absorption peak at 567 cm^{-1} that is potentially attributable to the deformation vibration of the Ti-O bond [43]. The absorption peaks at 3,445, 3,443, and 3,434 cm^{-1} and at 1,632, 1,624, and 1,602, cm^{-1} are attributable to the presence of external water and potential hydrogen-bonded OH in the $Ti_3C_2T_x$, SA_{20}, and MX-$SA_{4:20}$, respectively [44]. Following Hg^{2+} adsorption, the spectral peak at 3,434 cm^{-1}

is displaced to a lower angle at 3,423 cm^{-1}. The C-O and Na-O peaks at 1,034 and 821 cm^{-1}, respectively, in MX-$SA_{4:20}$, are the representative peaks of sodium alginate and are also shifted to lower angles following adsorption of Hg^{2+}.

Nitrogen gas sorption isotherms at 77.3 K corresponding to the calculated specific surface areas (BET) of 13.54, 9.23, and 9.66 m^2/g were collected for the $Ti_3C_2T_x$ MXene, SA_{20}, and MX-$SA_{4:20}$ spheres, respectively (Fig. S7A). The pore size distributions were calculated using density functional theory and found to be indicative of a hierarchical porosity from 2 to 6 nm in MX-$SA_{4:20}$ that can offer high accessibility to binding sites (Fig. S7B). TGA of the synthesized MX-$SA_{4:20}$ spheres was performed at 10 $^oC\ min^{-1}$ in a nitrogen atmosphere from ambient temperature to 1,000 ^oC. In the process, thermal degradation of MX-$SA_{4:20}$ occurred in five stages (Fig. 2D). A thermal degradation of 11.91% occurred between 23–160 ^oC (stage-I) as a result of loss of adsorbed water. Further decomposition occurred continuously across the applied temperature range, with a weight loss of up to 54.69% between 160–204 ^oC followed by more gradual weight reductions of 13.27, 2.988, and 4.376% from 204–400, 400–550, and 550-1,000 ^oC, respectively.

3.2. Mercuric ion capture and kinetics

The effectiveness of the synthesized materials was assessed through an analysis of their abilities to capture mercuric ions from an aqueous solution. For comparison with an identical 2-D nanomaterial that is potentially comparable to 2-D MXenes, a solution of GO and alginate was mixed into $CaCl_2$ to synthesize GO-$AS_{4:20}$ spheres. For further comparison with MX-$SA_{4:20,}$ additional alginate spheres (SA_{20}) were also synthesized. The MX-$SA_{4:20}$ was found to have an adsorption efficiency (100%) superior to those of both GO-$AS_{4:20}$ and SA_{20}, which had quantitative efficiencies of 34.63 and 11.53%, respectively (Fig. 3). Graphene oxide possess similar features likewise MXene, but intrinsic properties of graphene oxide show lack of surface functional groups available to metal ions [45]. On the other hand, $Ti_3C_2T_x$ MXene has superiority over graphene oxide owing to its hydrophilic nature, functional groups, and chemical stability. Especially, MX-

$SA_{4:20}$ spheres offered unique spherical structures (Fig. 1), which act like a cage to entrap Hg^{2+} ions and provide large available binding sites. The adsorption capacity of MX-$SA_{4:20}$ for Hg^{2+} was highest among those similar 2D graphene oxide and their derivatives (Table S4) [46-48].

Four different adsorbents—SA_{20} (without MXene), MX-$SA_{1:20,}$ MX-$SA_{2:20}$, and MX-$SA_{4:20}$—were added to a Hg^{2+}-contaminated solution (17.55 ppm) to compare their respective adsorption kinetics for Hg^{2+} capture (Fig. S8). The decreases in adsorption equilibrium time were found to be directly proportional to the MXene concentration, while the alginate concentrations remained constant up to a concentration ratio of 4:20% (MX-$SA_{4:20}$). As shown in Fig. 4A, particularly fast adsorption kinetics was observed for the MX-$SA_{4:20}$ spheres, with a 90% metal ion diffusion occurring in only 60 min and complete removal by 120 min. By contrast, the removal efficiencies of MX-$SA_{1:20}$ and MX-$SA_{2:20}$ were ∼44 and ∼72%, respectively, over 120 min (Fig. S8). The enhanced Hg^{2+} adsorption by MX-$SA_{4:20}$ can be credited to the porous structure of its spheres, its high specific surface, the unique functionality of MXene nanosheets in alginate, and the readily available functional groups for bonding with M^{2+} (OH, O, etc.) found in $Ti_3C_2T_x$ MXene.

Regeneration tests were then performed using HCl. An Hg^{2+}-laden MX-$SA_{4:20}$ sample was dissolved into 2, 4, 6, and 8 M HCl, kept under agitation for 5 h, and then analyzed via ICP-OES. The desorption results at different HCl concentrations are shown in Fig. S10, from which only 8 M HCl was capable of almost complete (99.69%) desorption of adsorbed Hg^{2+}. Therefore, an extreme acidic condition was required to desorb mercury ions from MX-$SA_{4:20}$ surfaces. In the literature, layered hydrogen metal sulfides and metal-organic frameworks showed similar desorption characteristics [49,50]. The regeneration of layered hydrogen metal sulfides after Hg loading required about 12 M HCl solutions [49]. In case of metal organic frame works, the Cd^{2+} ions adsorbed onto FJI-H9 could not leached out easily, required 16 M HNO_3 for reconstruction of structure and desorption of Cd^{2+} [50].

Adsorption kinetics models were then applied to carry out adsorption kinetics predictions using linearized Lagergren pseudo first- and second-order kinetic model equations (details on these

equations are given in Supplementary Information). The experimental data were well fitted to the pseudo second-order kinetic model (inset Fig. 4A), suggested that the rate determining step of Hg^{2+} adsorption onto MX-$SA_{4:20}$ and MX-$SA_{2:20}$ was primarily chemical (Table S2).

A further assessment of rapid decontamination ability for practical applications was carried out by reacting 3.32 ppm Hg^{2+} in tap water with MX-$SA_{4:20}$. At various intervals, aliquots were extracted from the mixture and measured using inductively coupled plasma-mass spectrometry. Within 15 min, the Hg^{2+} concentration was 1.8 ppb, which is below the US Environmental Protection Agency permissible limit of 2 ppb (Fig. 4B). This result suggests possible applications of MX-$SA_{4:20}$ for, e.g., the instant treatment of water contaminated by mercuric ions. The equilibrium Hg^{2+} adsorption capacity of MX-$SA_{2:20}$ and MX-$SA_{4:20}$ increased rapidly in the low concentration range (25–500 ppm), with the rate of increase slowing from 700–1,000 ppm before finally attaining maximum equilibrium capacities of 269.46 and 494.40 mg/g, respectively. For comparison with previously reported benchmark materials, distribution coefficient (k_d^{Hg}) values, as given by Eq. S5 in Supplementary Information, were calculated at a 500-ppm initial Hg^{2+} concentration. The results for MX-$SA_{4:20}$ were found to be as high as or higher than most of the reported benchmark values, with a k_d^{Hg} value of 8.75×10^7 mL/g (Fig. 5A). Attempts to use phosphate buffers (1.0 and 0.5 molar) at pH values of 6.5 were thwarted by the instability of the MX-$SA_{4:20}$ spheres in these solutions. In this case, Ca^{2+} in the solution reacted with $HPO4^{2-}$, creating $CaHPO_4$ precipitation [51], which resulted in the disintegration of the spheres (Fig. S9). The use of sodium maleate (1.0 and 0.5 M) buffer also resulted in breakdown of the MX-$SA_{4:20}$. Therefore, a stock solution prepared in DI water with a pH of ~4.5 was maintained for each concentration.

To further evaluate the mobility of Hg^{2+} ions onto the slid-phase adsorbent in aqueous solution, adsorption isotherm models were developed, with the Langmuir, Freundlich, and Redlich-Peterson adsorption isotherm approaches (Supplementary Information) used to simulate the adsorption isotherm of the system. The behavior of Hg^{2+} adsorption onto the MX-$SA_{4:20}$ spheres was found to fit best with the non-linear Redlich-Peterson adsorption isotherm (Fig. 5B), which is a combination

of the Langmuir and Freundlich isotherms [52]. The high value (>1) of the constant g (3.55) in the system suggested a multilayer-type adsorption process that was obviously well-suited to treatment using the Freundlich isotherm model. The maximum adsorption capacities calculated by the Langmuir isotherm model were 346.52 and 932.84 mg/g for MX-$SA_{2:20}$ and MX-$SA_{4:20}$, respectively (Table S3). The differences between the actual equilibrium adsorption capacities and the simulated maximum capacities calculated by the Langmuir isotherm model reflected the role of the multilayered $Ti_3C_2T_x$ MXene nanosheets in the MX-$SA_{4:20}$ dynamics. The isotherm models suggested that multilayer adsorption plays the primary role in the adsorption of Hg^{2+} onto the MX-$SA_{4:20}$ spheres.

3.3. pH effect

The effect of pH on the Hg^{2+} adsorption efficiency of MX-$SA_{4:20}$ was also assessed by adsorbing Hg^{2+} solution (25 ppm) onto MX-$SA_{4:20}$ (40 mg) at various pH values (2–11) at 25 ^{o}C. The results (Fig. 6) showed an exceptionally high quantitative removal of mercuric ions over the entire pH range. With a high removal efficiency under highly acidic conditions (~96% removal of Hg^{2+} at pH 2) and a complete capture of mercuric ions between pH 7–10 were found, although a slight decrease in removal efficiency (~98%) was observed in more basic environments (pH 11). The Hg^{2+} adsorption capability of MX-$SA_{4:20}$ under extreme acidic conditions was also notable: in the presence of 0.5 and 1 M HNO_3, MX-$SA_{4:20}$ could remove 88.13 and 86.39%, respectively, of the total Hg^{2+} (25 ppm) from the aqueous solution. The experimentally determined k_d^{Hg} values at high HNO_3 concentrations were unprecedented (9.29×10^3 and 8.01×10^3 mL/g for 0.5 and 1.0 M HNO_3, respectively). It was found that, in extremely concentrated acidic solutions (3 M HNO_3), the outer shells of the MX-$SA_{4:20}$ spheres were partially dissolved, which changed the solution color to a pale yellow. At HNO_3 concentrations of 1 M, by contrast, the MX-$SA_{4:20}$ spheres were stable. The stability of the inner core structures of the spheres under even extremely acidic conditions helped account for their high adsorption of Hg^{2+}; another potential adsorbent form for such extreme

acidic environments is the 3-D MXene-alginate gel-like structure. Previously, adsorption affinity toward Hg^{2+} over a broad pH range had only been reported for thiol-functional materials [53,54], and layered hydrogen metal sulfide [45]. The results reported here suggest the potential usefulness of MX-$SA_{4:20}$ spheres in the remediation of mercury in extreme acidic wastewater conditions such as the removal of mercury from nuclear waste.

3.4. Multiple element performance

Given that wastewater can hold multiple metal contaminants, further batch and breakthrough tests were performed to investigate the simultaneous removal of diverse metal ions. MX-$SA_{4:20}$ demonstrated good multi-component adsorption performance for nine toxic heavy metals ions, including soft (Hg^{2+} and Cd^{2+}), hard (Cr^{3+} and As^{3+}), and borderline Lewis metal ions (Pb^{2+}, Cu^{2+}, Zn^{2+}, Ni^{2+}, and Co^{2+}). In a typical batch experiment, MX-$SA_{4:20}$ performed remarkably well in removing >90 and >80% of five and three of the tested metal ions, respectively, although only 37% of the arsenic (As^{3+}) was removed (Fig. 7A). The presence of As^{3+}, or arsenite, depends highly on the pH of the solution, the nature of the adsorbent, and the functional group types. At an acidic pH, i.e., pH = 4.67, arsenite shows lower affinity for oxygenated and carboxylic host groups than Cr^{3+}, which exhibits high adsorption at lower pH because $HCrO_4^-$ is more easily adsorbed over a protonated surface [55]. These results indicate the high affinity of MX-$SA_{4:20}$ toward all types of metals ions. Even in the presence of competitive metal ions, the Hg^{2+} adsorption efficiency was still remarkably high, with a 99% removal rate; this was second only to Cd^{2+}, which was completely removed. The breakthrough experiment was carried out using an upflow column in which the bed was packed with MX-$SA_{4:20}$ and subjected to a flow rate of 0.3 mL/min. At the conclusion of the experiment, the terminal concentrations of eight metal ions were all decreased from 3 ppm to very low (detectable) levels. The results are shown in Fig. 7B; once again, the breakthrough time (taken as C/C_0=0.1) of Hg^{2+} appeared at one before the last (Cd^{2+}), indicating a good Hg^{2+} adsorbing capacity of MX-$SA_{4:20}$. Metal organic frameworks have only reported such exceptional adsorption

behaviors toward heavy metal ions adsorption [2]. Overall, the outcomes of these experiments reveal the ability of MX-$SA_{4:20}$ to perform very well with respect to Hg^{2+} adsorption in a competitive environment while simultaneously purifying multiple metal contaminants.

3.5. Analysis of removal mechanisms

The aqueous phase Hg^{2+} removal ability of MX-$SA_{4:20}$ spheres is driven by multiple mechanisms, including complex formation, ion-exchange, and electrostatic interaction. The inner-surface complexation between $[Ti{-}O]^{-}H^{+}$ and Hg^{2+} and ion exchange reaction between Ca^{2+} and Hg^{2+} are believed to be involved in adsorption of Hg^{2+}. The porous structure of sphere was beneficial for metal ion capturing during adsorption process. The hydroxyl (−OH), alkanes (−CH), and carboxyl (−COO) groups of biopolymer alginate also played an important role in adsorption mechanism. The hydroxyl and carboxylate groups from alginate are well known for heavy metal binding groups [52]. Further, the formation of $[Ti{-}O]^{-}H^{+}$ and $[Ti{-}O]^{-}Ca^{+}$ binding groups are predicted in MX-$SA_{4:20}$. The binding group $[Ti{-}O]^{-}H^{+}$ demonstrated strong metal-ligand interaction with Hg^{2+} [53]. Furthermore, the formation of $[Ti{-}O]^{-}Ca^{+}$ group during synthesis processes was also believed to be favorable for the enhancement in Hg^{2+} uptake.

The multi-layered and spontaneous Hg^{2+} adsorption processes were predicted using isotherms and kinetics models and XPS spectra of MX-$SA_{4:20}$, before and after adsorption of Hg^{2+} were analyzed to gain a better understanding of the removal mechanism (Scheme I). The XPS wide spectra scans indicated the presence of $Ti_3C_2T_x$ MXene and alginate representative peaks (Ti_{2p}, C_{1s}, F_{1s}, O_{1s}, Ca_{1s}, and Cl_{1s}) in the MX-$SA_{4:20}$. Following the adsorption of Hg^{2+}, peaks emerged in the Hg^{2+}@MX-$SA_{4:20}$ sample spectra (Fig. 2B) that demonstrated the immobilization of Hg on the surface of the MX-$SA_{4:20}$. The Hg^{2+}@MX-$SA_{4:20}$ Hg_{4f} spectrum peaks at $4f_{7/2}$ and $4f_{5/2}$ with binding energies of 100.36 and 104.43 eV, respectively, and divided by a spin orbit splitting of 4.07 eV might be attributable to HgO [31]. Additionally, the structural changes in the O_{1s} spectrum in Hg^{2+}@MX-$SA_{4:20}$ suggests an oxidation process between O^{-} and Hg^{2+}. During Hg^{2+} removal

processes, the amount of hydroxyl groups on the MX-$SA_{4:20}$ decreased progressively and the shift in binding energies of the peaks in the O_{1s} region to lower angles also suggested Hg^{2+} adsorption on MX-$SA_{4:20}$ (Table S1). In addition, a significant shift in Ti 2p to higher binding energy was observed (Fig. S4), confirming the presence of strong interaction between Hg^{2+} and Ti−O. In previous studies, the authors found reductive adsorption of Cu^{2+} by $Ti_3C_2T_x$ MXene nanosheets in which Cu^{2+} was partially reduced to Cu^{+} and formed cupric and cuprous oxides [54]. However, neither $Ti_3C_2T_x$ nor composites of $Ti_3C_2T_x$ MXene can reduce Hg^{2+} ions [31], indicating that the Hg^{2+} removal onto MX-$SA_{4:20}$ was controlled only by adsorption.

4. Conclusion

In this study, a safer route for synthesizing 2-D $Ti_3C_2T_x$ MXene using NH_4F instead of dangerous hydrofluoric acid was developed and a novel adsorbent, spherical MX-$SA_{4:20}$, was fabricated using a facile synthesis method involving 2-D $Ti_3C_2T_x$ MXene and SA networking. The core-shell of the MX-$SA_{4:20}$ sphere was found to be capable of very effectively removing Hg^{2+} ions from aqueous solution. The structure of MX-$SA_{4:20}$ was characterized using optical microscopic, SEM, XRD, FT-IR, and XPS imaging to determine its morphological, structural, and surface properties. Analysis of the synthesis and characterization of the MX-$SA_{4:20,}$ adsorption behavior of Hg^{2+}, and the effects of other toxic heavy metals on Hg^{2+} removal revealed that the primary adsorption mechanisms of metal ions onto MX-$SA_{4:20}$ are the host-guest inclusion of $[Ti{-}O]^{-}H^{+}$, functional groups on biopolymer alginate, and porous structures of the spheres. Batch and column testing of MX-$SA_{4:20}$ revealed that it could efficiently and simultaneously reduce single and multi-component metallic ion concentrations from high to environmental levels. MX-$SA_{4:20}$ performed excellently in extreme acidic conditions (pH <0) with an affinity and binding capacity for Hg^{2+} that reached or surpassed those of the most efficient known mercury adsorbents. The $Ti_3C_2T_x$ MXene nanosheets, which extended the adsorption capacity of the alginate spheres, also exhibited unique structures. The authors believe that the sphere fabrication process using 2D MXenes can be

extended and scaled to enable large-scale synthesis for multiple pollutant remediation's at an industrial level.

Conflict of interest

There are no conflicts to declare

Acknowledgments

This work was supported by LG Yonam Foundation (of Korea). This research was also supported by the Basic Science Research Program through the National Research Foundation of Korea (NRF) funded by the Ministry of Education and the Ministry of Science and ICT (NRF-2018R1A6A1A03024962, NRF-2018M2A7A1074563, and NRF-2016R1A2B4010431).

References

[1] K. Bakker, Water Security: Research Challenges and Opportunities, Science (80-.). 337 (2012) 914–915.

[2] Y. Peng, H. Huang, Y. Zhang, C. Kang, S. Chen, L. Song, et al., A versatile MOF-based trap for heavy metal ion capture and dispersion, Nat. Commun. 9 (2018) 1–9.

[3] P. Shao, J. Tian, F. Yang, X. Duan, S. Gao, W. Shi, et al., Identification and Regulation of Active Sites on Nanodiamonds: Establishing a Highly Efficient Catalytic System for Oxidation of Organic Contaminants, Adv. Funct. Mater. 28 (2018) 1–8.

[4] A. Shahzad, W. Miran, K. Rasool, M. Nawaz, J. Jang, S.-R. Lim, et al., Heavy metals removal by EDTA-functionalized chitosan graphene oxide nanocomposites, RSC Adv. 7 (2017) 9764–9771.

[5] X. Luo, T. Shen, L. Ding, W. Zhong, J. Luo, S. Luo, Novel thymine-functionalized MIL-101 prepared by post-synthesis and enhanced removal of Hg2+from water, J. Hazard. Mater. 306 (2016) 313–322.

[6] U.N. Environmental, Global mercury assessment, 2002.

[7] R.P. Mason, G.-R. Sheu, Role of the ocean in the global mercury cycle, Global Biogeochem. Cycles. 16 (2002) 40-1-40–14.

[8] D. Malakoff, Mercury pollution. Taming a mercurial element., Science. 341 (2013) 1442–1443.

[9] D.S. Tavares, C.B. Lopes, A.L. Daniel-da-Silva, C. Vale, T. Trindade, M.E. Pereira, Mercury in river, estuarine and seawaters – Is it possible to decrease realist environmental concentrations in order to achieve environmental quality standards?, Water Res. 106 (2016) 439–449.

[10] R.A. Bernhoft, Mercury toxicity and treatment: A review of the literature, J. Environ. Public Health. 2012 (2012) 1–10.

[11] Y. Zou, X. Wang, A. Khan, P. Wang, Y. Liu, A. Alsaedi, et al., Environmental remediation and application of nanoscale zero-valent iron and its composites for the removal of heavy metal ions: A review, Environ. Sci. Technol. 50 (2016) 7290–7304.

[12] A.P. Davis, P.M. Gietka, Removing Heavy Metals from Wastewater, 1994.

[13] and D.J. Ning Huang, Lipeng Zhai, Hong Xu, Stable Covalent Organic Frameworks for Exceptional Mercury Removal from Aqueous Solutions, J. Mater. Chem. A. 4 (2016) 11888–11896.

[14] X. Luo, C. Wang, L. Wang, F. Deng, S. Luo, X. Tu, et al., Nanocomposites of graphene oxide-hydrated zirconium oxide for simultaneous removal of As(III) and As(V) from water, Chem. Eng. J. 220 (2013) 98–106.

[15] H. Yu, P. Shao, L. Fang, J. Pei, L. Ding, S.G. Pavlostathis, et al., Palladium ion-imprinted polymers with PHEMA polymer brushes: Role of grafting polymerization degree in anti-interference, Chem. Eng. J. 359 (2019) 176–185.

[16] X. Min, X. Wu, P. Shao, Z. Ren, L. Ding, X. Luo, Ultra-high capacity of lanthanum-doped UiO-66 for phosphate capture: Unusual doping of lanthanum by the reduction of

coordination number, Chem. Eng. J. 358 (2019) 321–330.

[17] M.C. Dujardin, C. Cazé, I. Vroman, Ion-exchange resins bearing thiol groups to remove mercury. Part 1: Synthesis and use of polymers prepared from thioester supported resin, React. Funct. Polym. 43 (2000) 123–132.

[18] P. Hadi, M.H. To, C.W. Hui, C.S.K. Lin, G. McKay, Aqueous mercury adsorption by activated carbons, Water Res. 73 (2015) 37–55.

[19] Q. Sun, B. Aguila, J. Perman, L.D. Earl, C.W. Abney, Y. Cheng, et al., Postsynthetically Modified Covalent Organic Frameworks for Efficient and Effective Mercury Removal, J. Am. Chem. Soc. 139 (2017) 2786–2793.

[20] B. Li, Y. Zhang, D. Ma, Z. Shi, S. Ma, Mercury nano-trap for effective and efficient removal of mercury(II) from aqueous solution., Nat. Commun. 5 (2014) 1–7.

[21] F. Ke, L.G. Qiu, Y.P. Yuan, F.M. Peng, X. Jiang, A.J. Xie, et al., Thiol-functionalization of metal-organic framework by a facile coordination-based postsynthetic strategy and enhanced removal of Hg2+ from water, J. Hazard. Mater. 196 (2011) 36–43.

[22] J.D. Merrifield, W.G. Davids, J.D. MacRae, A. Amirbahman, Uptake of mercury by thiol-grafted chitosan gel beads, Water Res. 38 (2004) 3132–3138.

[23] A.J. Tchinda, E. Ngameni, I.T. Kenfack, A. Walcarius, One-step preparation of thiol-functionalized porous clay heterostructures: Application to Hg(II) binding and characterization of mass transport issues, Chem. Mater. 21 (2009) 4111–4121.

[24] B. Aguila, Q. Sun, J.A. Perman, L.D. Earl, C.W. Abney, R. Elzein, et al., Efficient Mercury Capture Using Functionalized Porous Organic Polymer, Adv. Mater. 29 (2017) 1–6.

[25] J. Li, X. Wang, G. Zhao, C. Chen, Z. Chai, A. Alsaedi, et al., Metal–organic framework-based materials: superior adsorbents for the capture of toxic and radioactive metal ions, Chem. Soc. Rev. 47 (2018) 2322–2356.

[26] M. Khajeh, S. Laurent, K. Dastafkan, Nanoadsorbents: Classification, preparation, and applications (with emphasis on aqueous media), Chem. Rev. 113 (2013) 7728–7768.

[27] M. Naguib, M. Kurtoglu, V. Presser, J. Lu, J. Niu, M. Heon, et al., Two-dimensional nanocrystals produced by exfoliation of Ti 3AlC 2, Adv. Mater. 23 (2011) 4248–4253.

[28] K. Rasool, M. Helal, A. Ali, C.E. Ren, Y. Gogotsi, Antibacterial Activity of Ti3C2Tx MXene, ACS Nano. 10 (2016) 3674–3684.

[29] R.P. Pandey, K. Rasool, V.E. Madhavan, B. Aïssa, Y. Gogotsi, K.A. Mahmoud, Ultrahigh-flux and fouling-resistant membranes based on layered silver/MXene (Ti3C2T:X) nanosheets, J. Mater. Chem. A. 6 (2018) 3522–3533.

[30] X. Guo, X. Zhang, S. Zhao, Q. Huang, J. Xue, High adsorption capacity of heavy metal with twodimensional MXenes: an ab initio study with molecular dynamics simulation, Phys. Chem. Chem. Phys. 18 (2015) 228–233.

[31] A. Shahzad, K. Rasool, W. Miran, M. Nawaz, J. Jang, K.A. Mahmoud, et al., Mercuric ion capturing by recoverable titanium carbide magnetic nanocomposite, J. Hazard. Mater. 344 (2018) 811–818.

[32] A. Shahzad, K. Rasool, M. Nawaz, W. Miran, J. Jang, Heterostructural TiO 2 / Ti 3 C 2 T x (MXene) for photocatalytic degradation of antiepileptic drug carbamazepine, Chem. Eng. J. 349 (2018) 748–755.

[33] V.M. Hong Ng, H. Huang, K. Zhou, P.S. Lee, W. Que, J.Z. Xu, et al., Recent progress in layered transition metal carbides and/or nitrides (MXenes) and their composites: synthesis and applications, J. Mater. Chem. A. 5 (2017) 3039–3068.

[34] A. Feng, Y. Yu, Y. Wang, F. Jiang, Y. Yu, L. Mi, et al., Two-dimensional MXene Ti3C2produced by exfoliation of Ti3AlC2, Mater. Des. 114 (2017) 161–166.

[35] C. Shen, L. Wang, A. Zhou, B. Wang, X. Wang, W. Lian, et al., Synthesis and Electrochemical Properties of Two-Dimensional RGO/Ti3C2Tx Nanocomposites, Nanomaterials. 8 (2018) 80.

[36] F. Liu, A. Zhou, J. Chen, J. Jia, W. Zhou, L. Wang, et al., Preparation of Ti3C2 and Ti2C MXenes by fluoride salts etching and methane adsorptive properties, Appl. Surf. Sci. 416

(2017) 781–789.

[37] N. Mohammed, N. Grishkewich, H.A. Waeijen, R.M. Berry, K.C. Tam, Continuous flow adsorption of methylene blue by cellulose nanocrystal-alginate hydrogel beads in fixed bed columns, Carbohydr. Polym. 136 (2016) 1194–1202.

[38] M. Sonmes, A. Ficai, E. Andronescu, Alginate/cellulose composite beads for environmental applications, UPB Sci. Bull. Ser. B Chem. Mater. Sci. 78 (2016) 165–176.

[39] L. Jin-Cheng, X. Zhang, Z. Zhou, Recent advances in MXene: Preparation, properties, and applications, Front. Phys. 10 (2015) 276–286.

[40] O. Mashtalir, M. Naguib, B. Dyatkin, Y. Gogotsi, M.W. Barsoum, Kinetics of aluminum extraction from Ti3AlC2 in hydrofluoric acid, Mater. Chem. Phys. 139 (2013) 147–152.

[41] Y. Zhuang, F. Yu, H. Chen, J. Zheng, J. Ma, J. Chen, Alginate/graphene double-network nanocomposite hydrogel beads with low-swelling, enhanced mechanical properties, and enhanced adsorption capacity, J. Mater. Chem. A. 4 (2016) 10885–10892.

[42] J. Halim, K.M. Cook, M. Naguib, P. Eklund, Y. Gogotsi, J. Rosen, et al., X-ray photoelectron spectroscopy of select multi-layered transition metal carbides (MXenes), Appl. Surf. Sci. 362 (2016) 406–417.

[43] Q. Peng, J. Guo, Q. Zhang, J. Xiang, B. Liu, A. Zhou, et al., Unique lead adsorption behavior of activated hydroxyl group in two-dimensional titanium carbide, J. Am. Chem. Soc. 136 (2014) 4113–4116.

[44] Q. Zhang, J. Teng, G. Zou, Q. Peng, Q. Du, T. Jiao, et al., Efficient phosphate sequestration for water purification by unique sandwich-like MXene/magnetic iron oxide nanocomposites, Nanoscale. 8 (2016) 7085–7093.

[45] M.J. Manos, V.G. Petkov, M.G. Kanatzidis, H2xMnxSn3-xS6 (x = 0.11-0.25): A novel reusable sorbent for highly specific mercury capture under extreme pH conditions, Adv. Funct. Mater. 19 (2009) 1087–1092.

[46] H. Xue, Q. Chen, F. Jiang, D. Yuan, G. Lv, L. Liang, et al., A regenerative metal-organic

framework for reversible uptake of Cd(II): From effective adsorption to: In situ detection, Chem. Sci. 7 (2016) 5983–5988.

[47] D.W. Newton, D.F. Driscoll, Calcium and phosphate compatibility: Revisited again, Am. J. Heal. Pharm. 65 (2008) 73–80.

[48] K. Rasool, D.S. Lee, Characteristics, kinetics and thermodynamics of Congo Red biosorption by activated sulfidogenic sludge from an aqueous solution, Int. J. Environ. Sci. Technol. 12 (2013) 571–580.

[49] K.H. Nam, L.L. Tavlarides, Mercury removal from acidic waste solutions using a thiol functional organo-ceramic adsorbent, Solvent Extr. Ion Exch. 21 (2003) 899–913.

[50] Y. Shin, G.E. Fryxell, W. Um, K. Parker, S. V. Mattigod, R. Skaggs, Sulfur-functionalized mesoporous carbon, Adv. Funct. Mater. 17 (2007) 2897–2901.

[51] N. Zhu, T. Yan, J. Qiao, H. Cao, Adsorption of arsenic, phosphorus and chromium by bismuth impregnated biochar: Adsorption mechanism and depleted adsorbent utilization, Chemosphere. 164 (2016) 32–40.

[52] N. Zhu, T. Yan, J. Qiao, H. Cao, Z. Tong, Y. Chen, et al., Preparation, Characterization and Properties of Alginate/Poly(γ-glutamic acid) Composite Microparticles, Mar. Drugs. 164 (2017) 32–40.

[53] J. GORDON E. BROWN, A.L. FOSTER, JOHN D. OSTERGREN, Mineral surfaces and bioavailability of heavy metals: A molecular-scale perspective, Proc. Natl. Acad. Sci. USA. 96 (1999) 3388–3395.

[54] A. Shahzad, K. Rasool, W. Miran, M. Nawaz, J. Jang, K. Mahmoud, et al., Two-Dimensional Ti3C2Tx MXene Nanosheets for Efficient Copper Removal from Water, ACS Sustain. Chem. Eng. 5 (2017) 11481–11488.

List of Figures

$SA_{4:20}$, demonstrating exceptional maximum adsorption capacities (Q_{max}) of 364.52 and 932.84 mg/g, respectively (calculated by Langmuir isotherm model).

Figure 6: Effect of pH on Hg^{2+} adsorption (quantitatively) on MX-$SA_{4:20}$ spheres. The k_d^{Hg} values in 1 and 0.5 M HNO_3 solution are 8.01×10^3 and 9.29×10^3 mL g^{-1}, respectively.

Figure 7: Adsorption performance of MX-$SA_{4:20}$ in multi-component system: (A) simultaneous adsorption of eight toxic metal ions in batch system (conditions: 50 mg adsorbent dose added to 30 mL aqueous solution containing 3 ppm of each metal ion, agitated for 24 h at pH; 4.67). (B) Breakthrough curve in fixed bed adsorption of multi-ions.

Scheme I: Graphical illustration of Hg^{2+} ions uptake onto MX-$SA_{4:20}$ spheres.

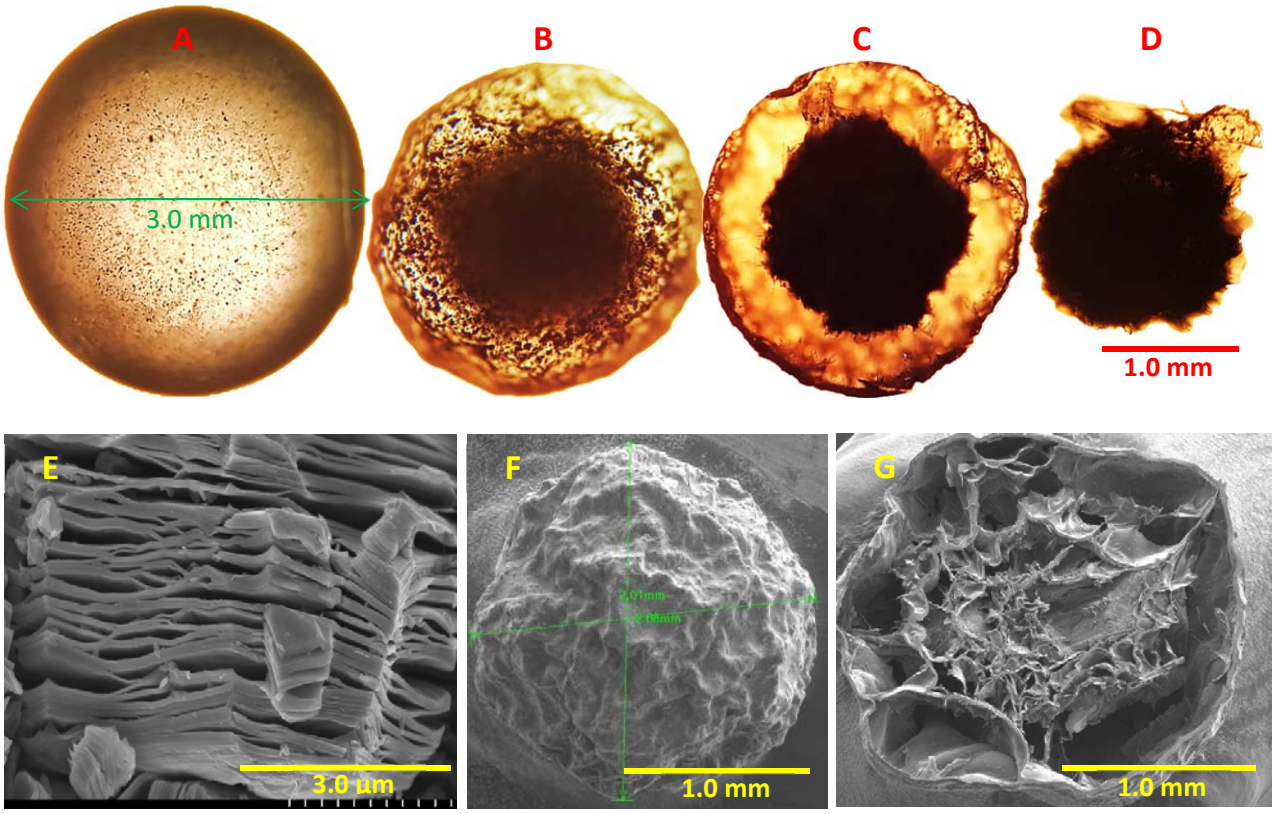

Figure 1

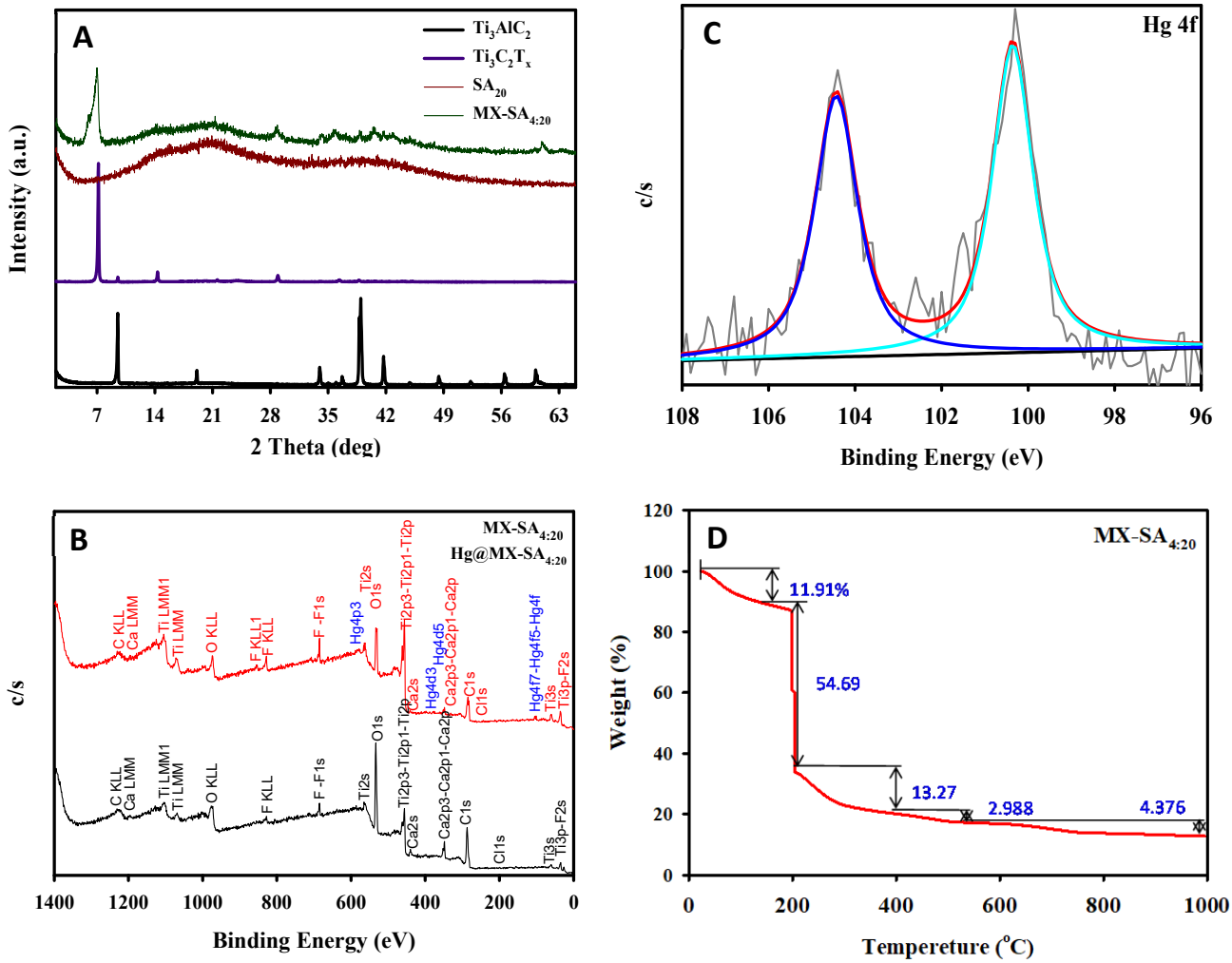
A
Ti3AlC2
Ti3C2Tx
SA20
MX-SA4:20
Intensity (a.u.)
2 Theta (deg)
C
Hg 4f
c/s
Binding Energy (eV)
B
MX-SA4:20
Hg@MX-SA4:20
c/s
Binding Energy (eV)
D
MX-SA4:20
11.91%
54.69
13.27
2.988
4.376
Weight (%)
Tempereture (°C)

Figure 2

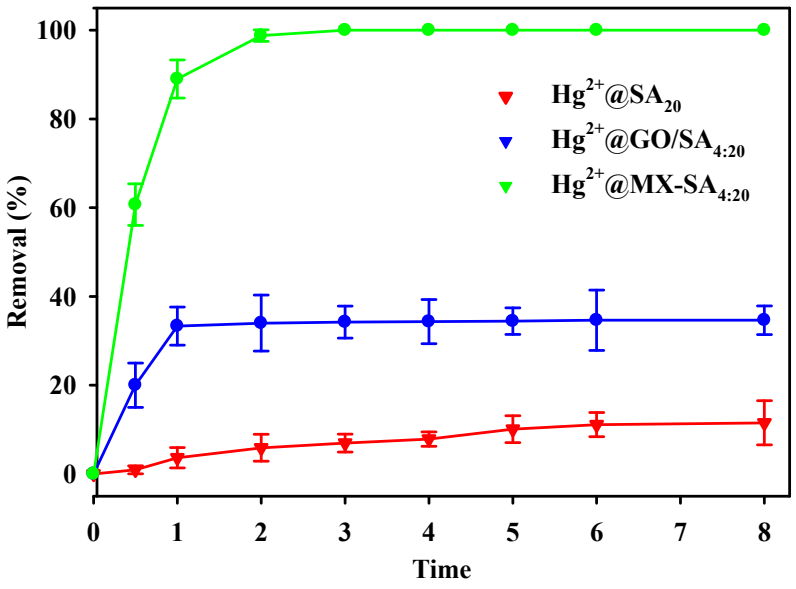
Removal (%)
Time
100
80
60
40
20
0
0
1
2
3
4
5
6
7
8
Hg2+@SA20
Hg2+@GO/SA4:20
Hg2+@MX-SA4:20

Figure 3

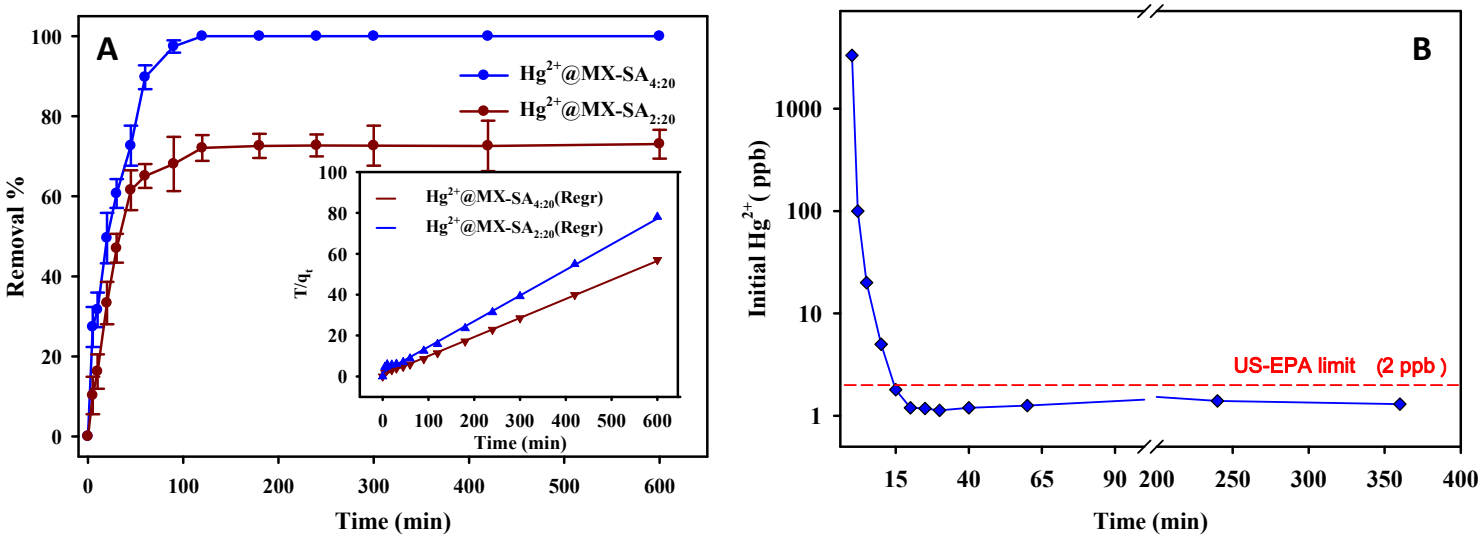
A
Removal %
Time (min)
Hg2+@MX-SA4:20
Hg2+@MX-SA2:20
Hg2+@MX-SA4:20(Regr)
Hg2+@MX-SA2:20(Regr)
T/qt
B
Initial Hg2+ (ppb)
US-EPA limit (2 ppb)

Figure 4

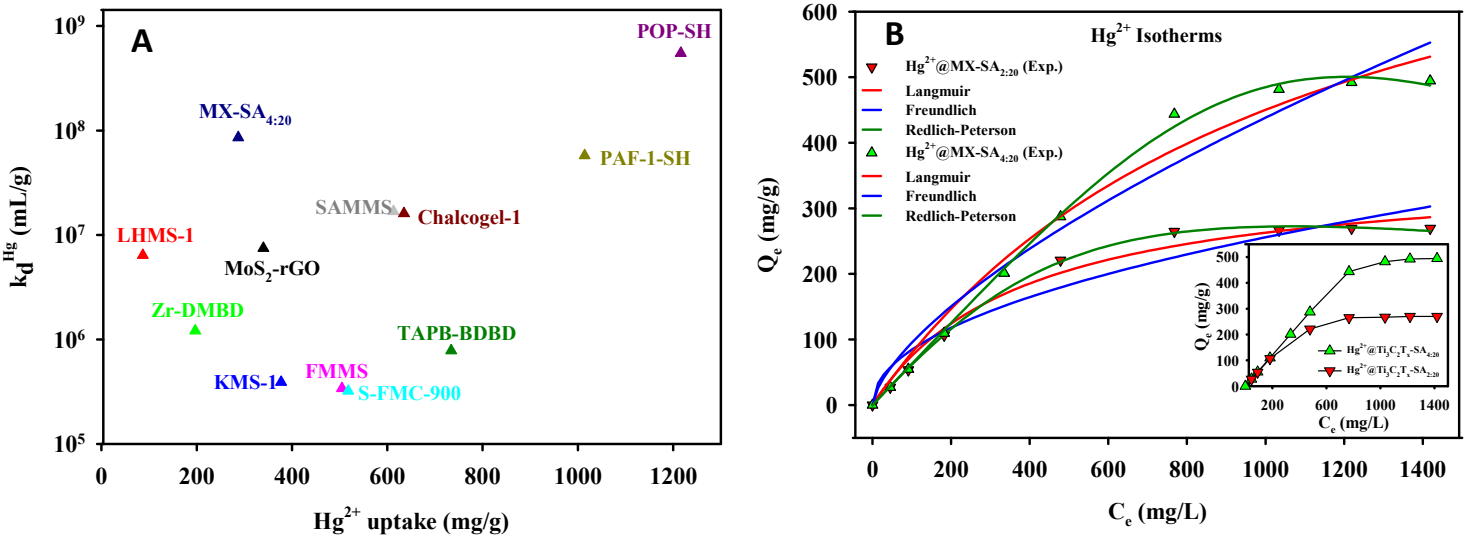
A
POP-SH
MX-SA4:20
PAF-1-SH
SAMMS
Chalcogel-1
LHMS-1
MoS2-rGO
Zr-DMBD
TAPB-BDBD
KMS-1
FMMS
S-FMC-900
Hg2+ uptake (mg/g)
B
Hg2+ Isotherms
Hg2+@MX-SA2:20 (Exp.)
Langmuir
Freundlich
Redlich-Peterson
Hg2+@MX-SA4:20 (Exp.)
Langmuir
Freundlich
Redlich-Peterson
Qe (mg/g)
Ce (mg/L)

Figure 5

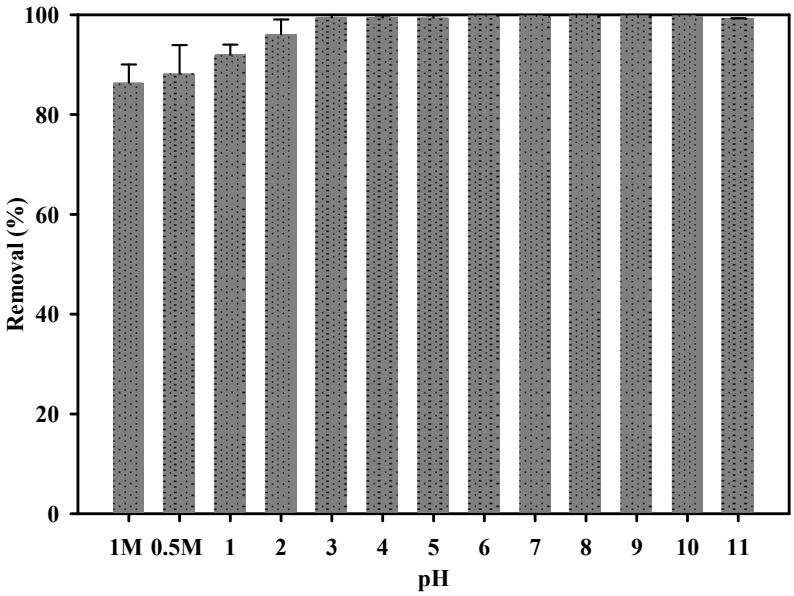

Figure 6

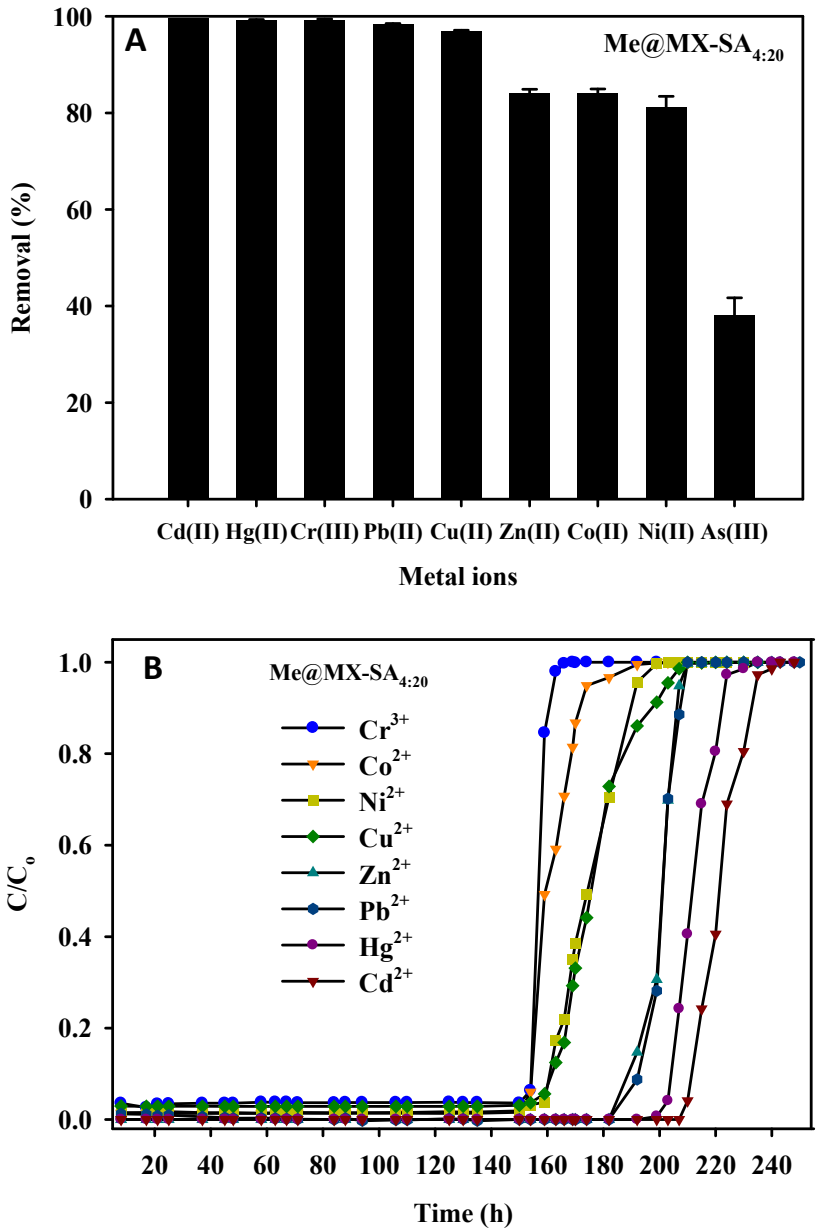
A
Me@MX-SA4:20
Removal (%)
100
80
60
40
20
0
Cd(II) Hg(II) Cr(III) Pb(II) Cu(II) Zn(II) Co(II) Ni(II) As(III)
Metal ions
B
Me@MX-SA4:20
Cr3+
Co2+
Ni2+
Cu2+
Zn2+
Pb2+
Hg2+
Cd2+
C/Co
1.0
0.8
0.6
0.4
0.2
0.0
20 40 60 80 100 120 140 160 180 200 220 240
Time (h)

Figure 7

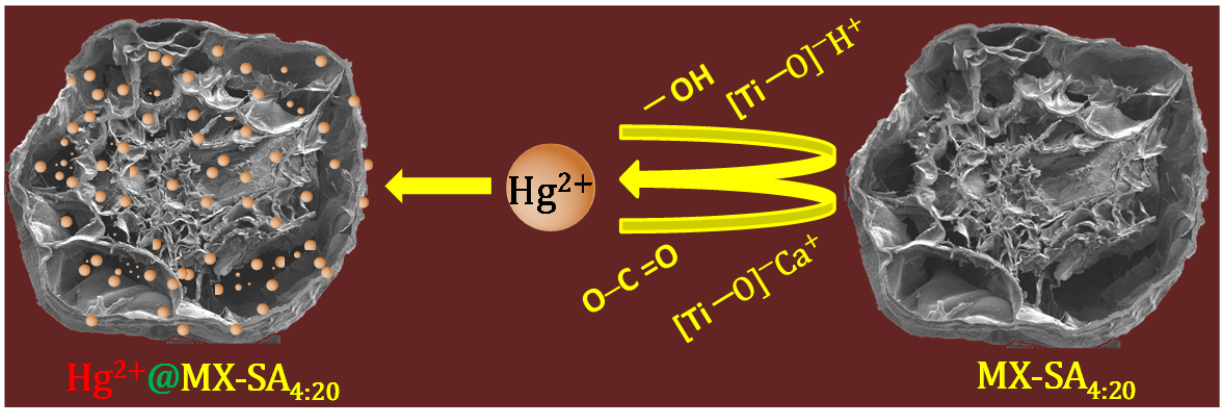

Scheme I

Supplementary Materials

$Ti_3C_2T_x$ MXene core-shell spheres for ultrahigh removal of mercuric ions

Asif Shahzad[1], Mohsin Nawaz[1], Mokrema Moztahida[1], Jiseon Jang[2], Khurram Tahir[1], Jiho Kim[1], Youngsu Lim[1], Vassilios S. Vassiliadis[3], Seung Han Woo[4,*] and Dae Sung Lee[1,*]

[1]*Department of Environmental Engineering, Kyungpook National University, 80 Daehak-ro, Buk-gu, Daegu 41566, Republic of Korea*

[2]*R&D Institute of Radioactive Wastes, Korea Radioactive Waste Agency, 174 Gajeong-ro, Yuseong-gu, Daejeon 34129, Republic of Korea*

[3]*Department of Chemical Engineering and Biotechnology, University of Cambridge, West Cambridge Site, Philippa Fawcett Drive, Cambridge CB3 0AS, UK*

[4]*Department of Chemical Engineering, Hanbat National University, 125 Dongseodae-ro, Yuseong-gu, Daejeon 34158, Republic of Korea*

*To whom all correspondence should be addressed.

Tel.: +82-53-953-7286; Fax: +82-53-950-6579

E-mail: daesung@knu.ac.kr & shwoo@hanbat.ac.kr

Supplementary note I

$$\text{Removal rate } \% = \frac{(C_o - C_t)}{C_o} \times 100\% \quad \text{(S1)}$$

$$Q_e = \frac{(C_o - C_e) \times V}{m} \quad \text{(S2)}$$

where C_o and C_t (mg/L) are the initial and final (at time t) concentrations of Hg^{2+}, respectively, V is the solution volume, m is the mass of adsorbent, and Q_e is the absolute sorption capacity at equilibrium

Adsorption Kinetics models for Hg(II)

$$\ln(Q_e - Q_t) = \ln Q_e - k_1 t \quad \text{(S3)}$$

where Q_t are the metal ion concentrations at time t and k_1 is the first-order rate constant (s^{-1}).

$$\frac{t}{Q_t} = \frac{1}{k_2 Q_e^2} + \frac{t}{Q_e} \quad \text{(S4)}$$

where k_2 represents the second-order rate constant (g/mg s); in this case, t/Q_t is plotted against t. The equilibrium rate constants of the linearized Lagergren pseudo first- and second-order kinetic models were expressed by plotting temperature T (K) against $\ln(q_e\text{-}q_t)$ and T/q_t, respectively.

Distribution coefficient for Hg(II)

$$k_d = \frac{(C_o - C_t)}{C_t} \times \frac{V}{m} \quad \text{(S5)}$$

where C_o (mg/L) is the initial concentration of Hg^{2+}, C_t (mg/L) is the concentration of Hg^{2+} after adsorption equilibrium, V (mL) is the solution volume, and m (mg) is the mass of MX-$SA_{4:20}$ used.

Adsorption Isotherm models for Hg(II)

Langmuir isotherm equation:

$$q_e = \frac{q_m K_a C_e}{1 + K_a C_e} \tag{S6}$$

Freundlich isotherm equation:

$$q_e = K_F C_e^{(\frac{1}{n})} \tag{S7}$$

Redlich-Peterson isotherm equation:

$$q_e = \frac{AC_e}{1 + BC_e^g} \tag{S8}$$

where q_e is the sorption capacity of MX-$SA_{4:20}$ at equilibrium, C_e is the equilibrium concentration of Hg(II) in solution, q_m is the maximum adsorption capacity, and K_a, K_F, n, A, B, and g are the isotherm constants for the Langmuir, Freundlich, and Redlich-Peterson adsorption isotherm model equations.

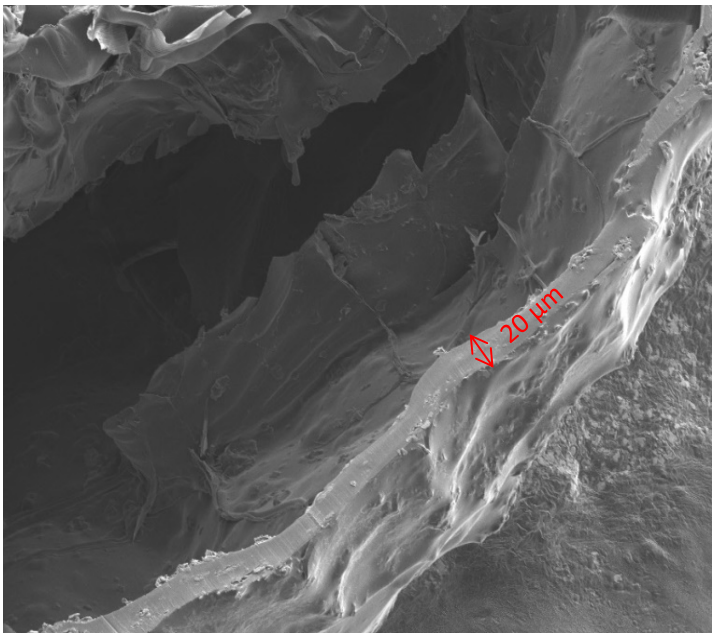

Figure S1. Outer shell wall of MX-$SA_{4:20}$ sphere.

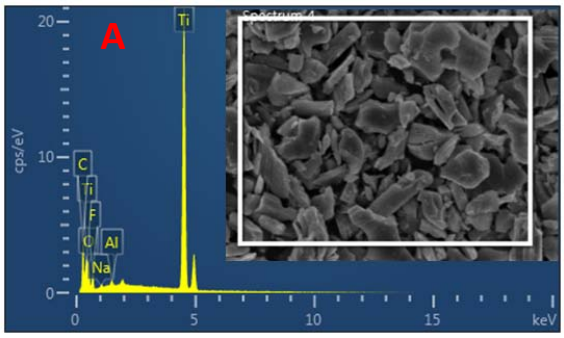

Element	Wt%	Atomic %
C (K)	11.31	11.31
O (K)	13.47	13.47
F (K)	8.19	8.19
Al (K)	0.42	0.42
Ti (K)	66.15	66.15
Total:	100.00	100.00

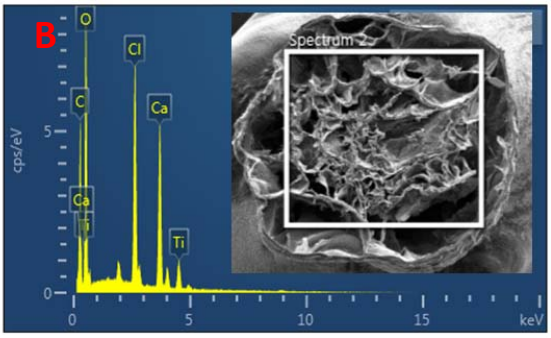

Element	Wt%	Atomic %
C (K)	34.60	47.66
O (K)	40.30	41.67
Cl (K)	9.99	4.66
Ca (K)	11.78	4.86
Ti (K)	3.32	1.15
Total:	100.00	100.00

Figure S2. SEM-EDS elemental composition of $Ti_3C_2T_x$ (A) and MX-$SA_{4:20}$ spheres (B). Following adsorption, aluminum and fluoride are completely removed from the MX-$SA_{4:20}$.

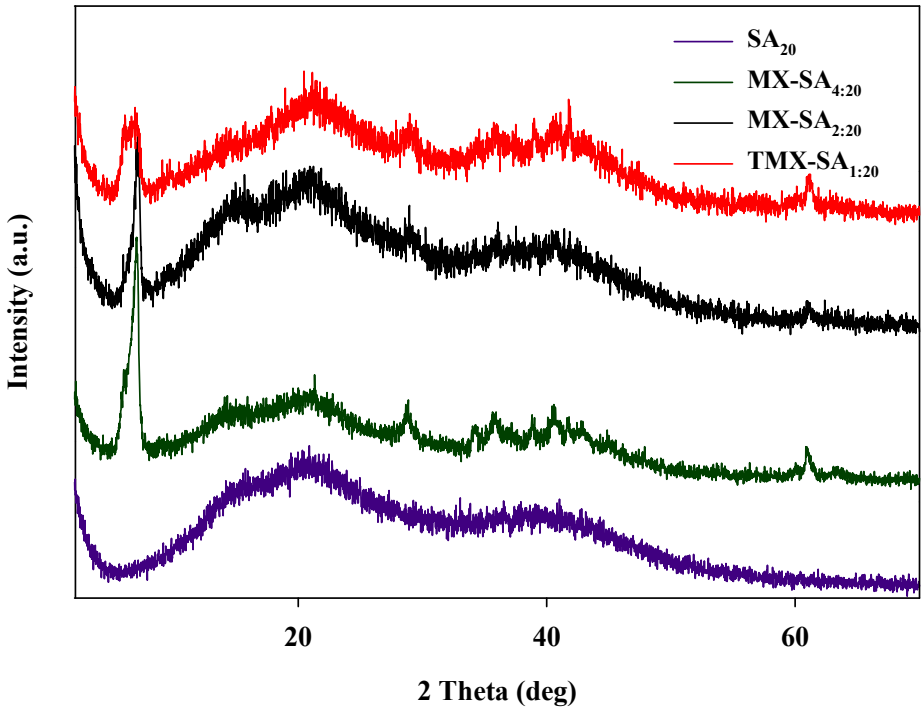

Figure S3. XRD spectra of SA_{20}, MX-$SA_{4:20}$, MX-$SA_{2:20}$, and M X-$SA_{1:20}$.

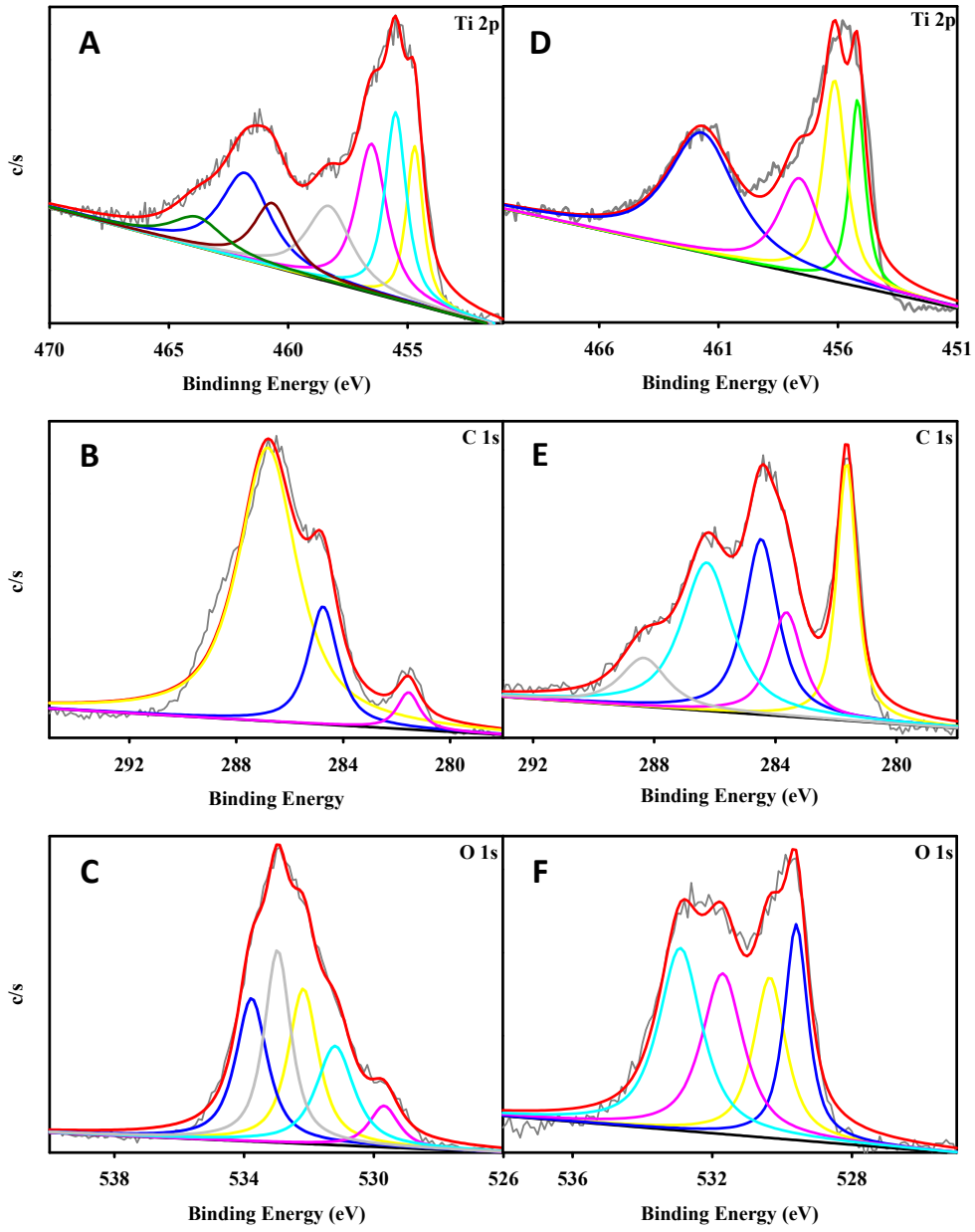

Figure S4. Pre- and post-adsorption component peak-fitting of XPS spectra. Prior to Hg^{2+} adsorption: (A) Ti 2p, (B) C 1s, and (C) O_{1s} of $MX/SA_{4:20}$ spheres. Following adsorption: (D) Ti_{2p}, (E) C_{1s}, and (F) O_{1s} of Hg^{2+}@$MX/SA_{4:20}$. These reflect the various moieties believed to exist in $MX/SA_{4:2}$ and Hg^{2+}@$MX/SA_{4:20}$.

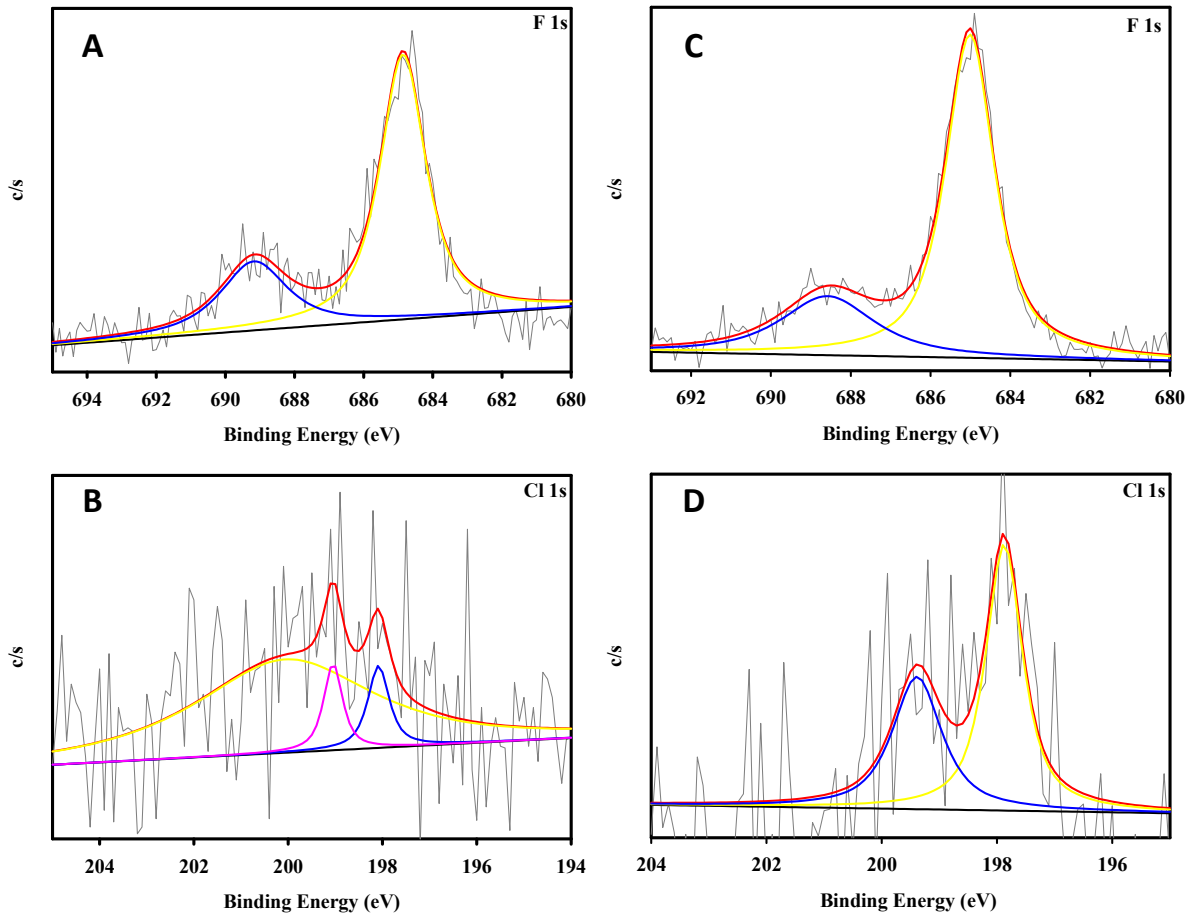

Figure S5. Pre- and post-adsorption components of peak-fitting XPS spectra. Prior to adsorption: (A) F_{1s}, and (B) Cl_{1s} of $MX/SA_{4:20}$ spheres. Post-adsorption: (C) F_{1s}, and (D) Cl_{1s} of Hg^{2+}@$MX/SA_{4:20}$.

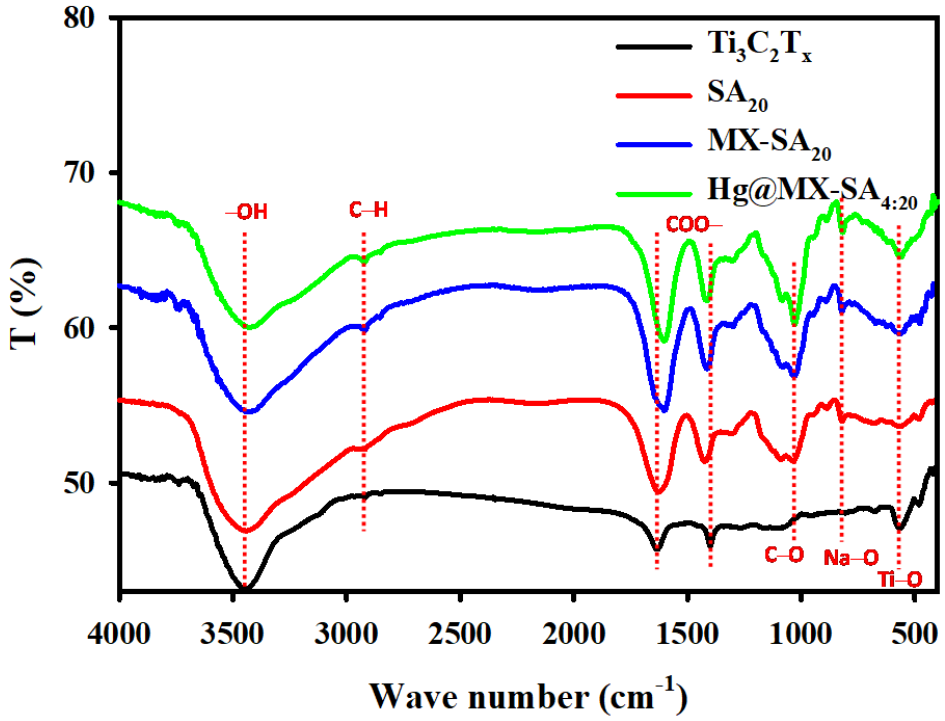

Figure S6 Fourier transform infrared (FTIR) spectra of $Ti_3C_2T_x$ MXene, SA_{20}, MX-$SA_{4:20}$, and Hg^{2+}@MX-$SA_{4:20}$

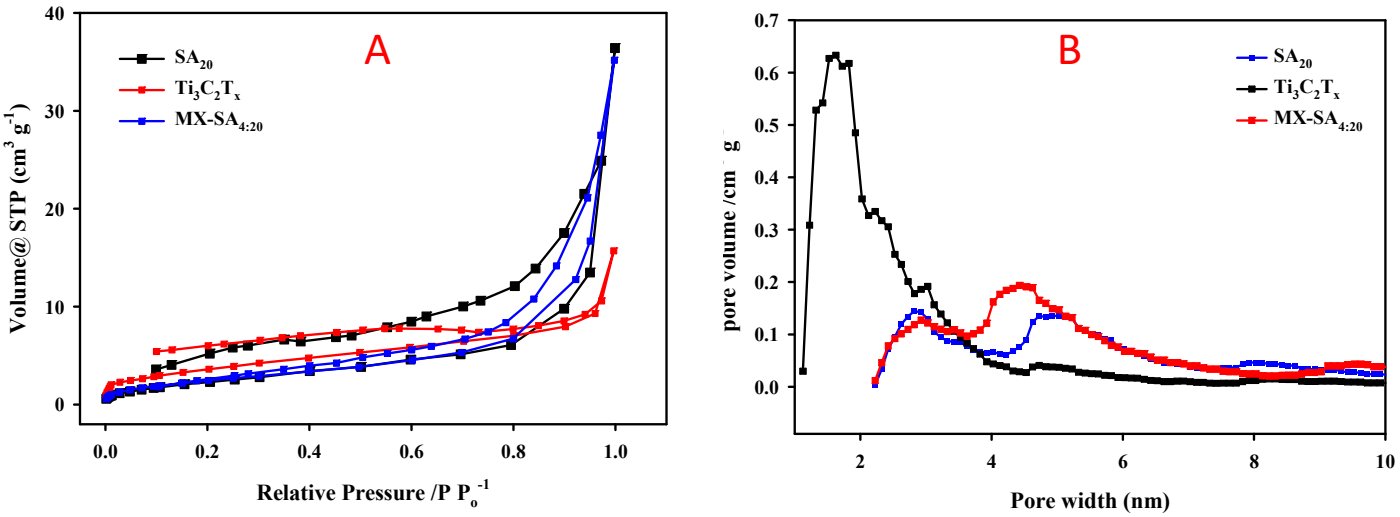

Figure S7. (A) Nitrogen adsorption–desorption isotherms and (B) pore size distributions calculated from N2 desorption isothermals for SA_{20}, $Ti_3C_2T_x$ MXene, and MX-$SA_{4:20}$.

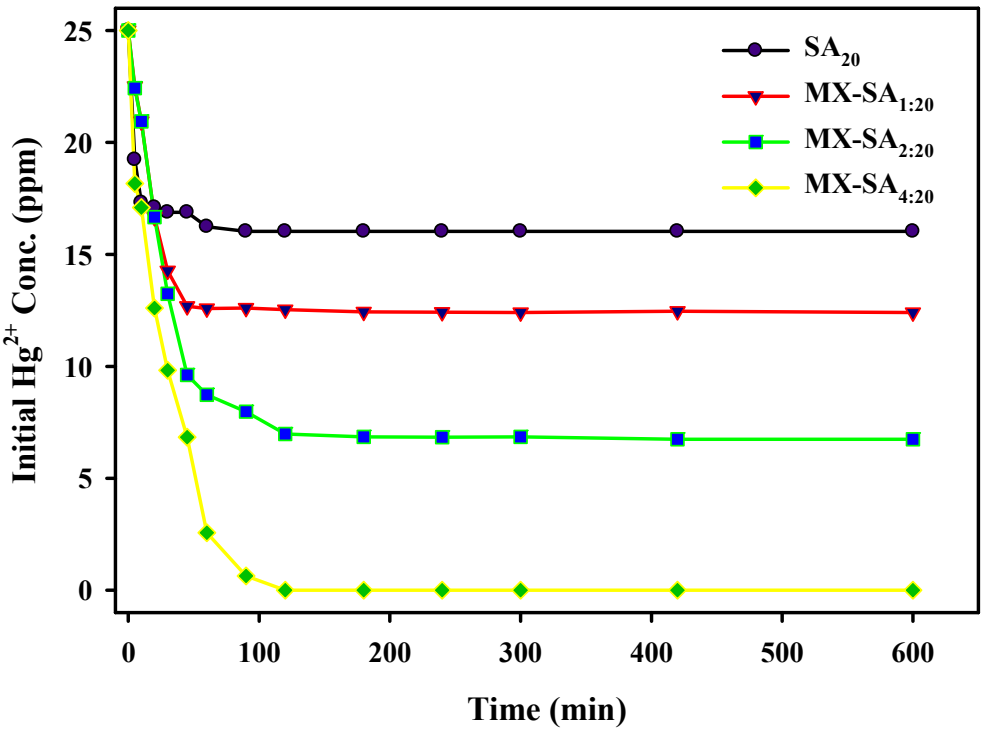

Figure S8. Hg^{2+} adsorption kinetics onto SA_{20}, MX-$SA_{1:20}$, MX-$SA_{2:20}$, and MX-$SA_{4:20}$ spheres.

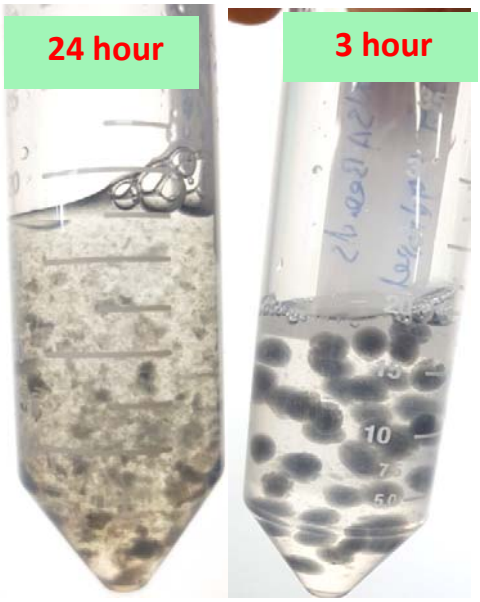

Figure S9. MX-$SA_{4:20}$ spheres in 1.0 M phosphate buffer solutions at different time intervals.

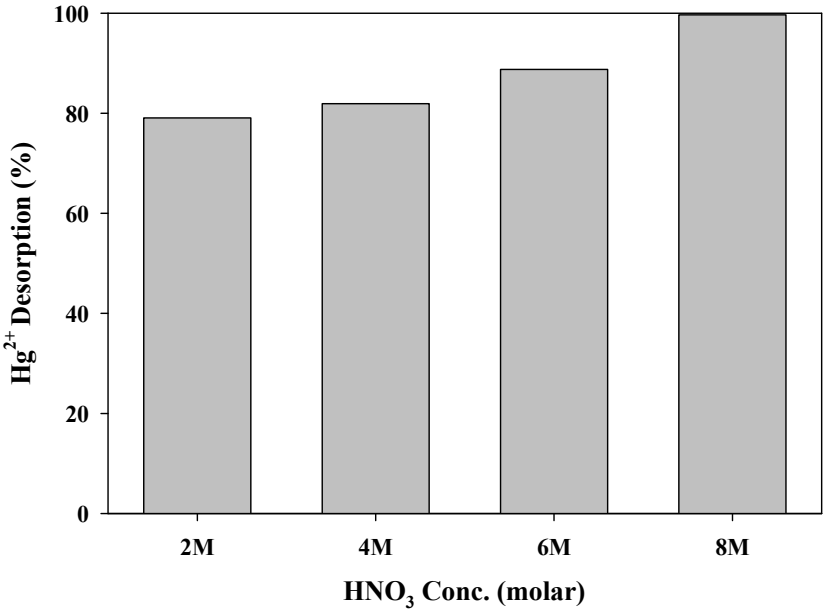

Figure S10. Desorption of adsorbed Hg^{2+} from Hg^{2+}@MX-$SA_{4:20}$ in HCl solution.

Table S1. MX-$SA_{4:20}$ sphere chemical compositions under different states

Adsorbent	1st order			2nd order			Experimental
	q_e (mg/g)	K_1 (g/mg/min)	r^2	q_e (mg/g)	K_2 (g/mg/min)	r^2	q_e (mg/g)
Hg^{2+}@MX/$SA_{2.20}$	6.16	-0.0029	0.746	7.99	0.12446	0.996	7.692
Hg^{2+}@MX/$SA_{4.20}$	2.58	-0.0027	0.213	10.75	0.034577	0.999	10.53

Table S2. Adsorption kinetics parameters of Hg^{2+} adsorption by $MX/SA_{2:20}$ and $MX/SA_{4:20}$

MXene Sample	Region	BE [eV]	Assigned to
MX-SA$_{4:20}$	*Ti 2p*	*454.7*	Ti (I, II, or IV)
		455.5 (461.8)	Ti^{2+} (I, II, or IV)
		456.51(463.8)	TiO_2
		458.29	TiO_2
		460.67	C–Ti–F_x (III)
	C 1s	286.83	C–O
		284.75	C–C or C=C
		281.56	C–Ti–T_x
	O 1s	529.64	TiO_2
		531.19	C–Ti–O_x (I) or OR
		532.18	C–Ti–$(OH)_x$ (II) and/or OR
		532.97	Cl–O^-
		533.77	H_2O_{ads} (IV) and/or OR
	F 1s	684.86	C–Ti–F_x (III)
		689.17	OR–F_x
	Cl 1s	198.08	Metal–Cl_x
		199.05	$CaCl_2$
		200.05	CH=CHCl$_x$
Hg^{2+}@MX-SA$_{4:20}$	*Ti 2p*	455.18	Ti (I, II, or IV)
		456.14 (461.7)	Ti^{2+} (I, II, or IV)
		457.61	Ti^{3+} (I, II, or IV)
		464.6	TiO_2
	C 1s	281.65	C–Ti–T_x
		284.47	C–O
		283.64	R–Al
		286.27	CH_x/C–O
		288.34	C=O
	O 1s	530.35	TiO_2
		529.59	TiO_2
		531.7	C–Ti– $(OH)_x$ (II) and/or OR
		532.61	C=O
	F 1s	685.01	C–Ti–F_x (III)
		688.58	OR–F_x
	Cl	197.88	Metal–Cl_x
		199.39	OR–Cl_x
	Hg 4f	100.36	HgO
		104.43	HgO

Table S3. Adsorption isotherm parameters of Hg^{2+} adsorption by $MX/SA_{2:20}$ and $MX/SA_{4:20}$ sphere

Isotherm	**Parameters**	**Hg^{2+}@MX/$SA_{2.20}$**		**Hg^{2+}@MX/$SA_{4.20}$**	
		Values	***R^2***	***Values***	***R^2***
Langmuir	q_{max} (mg/g)	364.52	0.982	932.84	0.981
	k_L	0.0026		0.000933	
Freundlich	k_F (mg/g)	9.19	0.933	4.45	0.959
	1/n	0.48		0.67	
Redlich-Peterson	A (L/mg)	0.632	0.999	0.628	0.997
	B (L/mg)	1.264×10^{-5}		4.299×10^{-7}	
	g	1.68		2.95	

Table S4. Comparison between two-dimenssional nanomaterials, cellulose and their darivatives with MX-$SA_{4:20}$.

Adsorbent	**Initial conc. (mg L^{-1})**	**Adsorption Capacity (mg g^{-1})**	**pH**	**Ref.**
Fe_3O_4-GS	5	23.03	6.0	[S1]
EDTA-mGO	50	268.40	4.1	[S2]
MGO	100	71.3	6	[S3]
PEI–PD/GO composite	50	110	4.0	[S4]
Spanish broom	100	20	6	[S5]
cellulose nanofibers (CNFs)	200	116.82	7	[S6]
Activate Carbon	20-50	16.15	5.0	[S7]
GO/mCS nanofilling	0-500	397	6.0	[S8]
CS/CNTs beads	1000	183.2	5	[S9]
MX-$SA_{4:20}$	31-993	932.84	4.5	This work

Reference

[S1] X. Guo, B. Du, Q. Wei, J. Yang, L. Hu, L. Yan, W. Xu, Synthesis of amino functionalized magnetic graphenes composite material and its application to remove Cr(VI), Pb(II), Hg(II), Cd(II) and Ni(II) from contaminated water, J. Hazard. Mater. 278 (2014) 211–220.

[S2] L. Cui, Y. Wang, L. Gao, L. Hu, L. Yan, Q. Wei, B. Du, EDTA functionalized magnetic graphene oxide for removal of Pb(II), Hg(II) and Cu(II) in water treatment: Adsorption mechanism and separation property, Chem. Eng. J. 281 (2015) 1–10.

[S3] Y. Guo, J. Deng, J. Zhu, X. Zhou, R. Bai, Removal of mercury(II) and methylene blue from a wastewater environment with magnetic graphene oxide: Adsorption kinetics, isotherms and mechanism, RSC Adv. 6 (2016) 82523–82536.

[S4] Z. Dong, F. Zhang, D. Wang, X. Liu, J. Jin, Polydopamine-mediated surface-functionalization of graphene oxide for heavy metal ions removal, J. Solid State Chem. 224 (2015) 88–93.

[S5] F.E. Arias Arias, A. Beneduci, F. Chidichimo, E. Furia, S. Straface, Study of the adsorption of mercury (II) on lignocellulosic materials under static and dynamic conditions, Chemosphere. 180 (2017) 11–23.

[S6] M. Bansal, B. Ram, G.S. Chauhan, A. Kaushik, L-Cysteine functionalized bagasse cellulose nanofibers for mercury(II) ions adsorption, Int. J. Biol. Macromol. 112 (2018) 728–736.

[S7] K. Kadirvelu, M. Kavipriya, C. Karthika, N. Vennilamani, S. Pattabhi, Mercury (II) adsorption by activated carbon made from sago waste, Carbon N. Y. 42 (2004) 745–752.

[S8] G.Z. Kyzas, N.A. Travlou, E.A. Deliyanni, The role of chitosan as nanofiller of graphite oxide for the removal of toxic mercury ions, Colloids Surfaces B Biointerfaces. 113 (2014) 467–476.

[S9] S. Hosam A, E.-A. Abdel Hameed M., A.-Z. Dalia E., Chitosan/Carbon Nanotube Composite Beads: Preparation, Characterization, and Cost Evaluation for Mercury Removal from Wastewater of Some Industrial Cities in Egypt, J. Appl. Polym. Sci. 25 (2012) E93–E101.